Journal of Power Sources 587 (2023) 233707

Contents lists available at ScienceDirect

Journal of Power Sources

journal homepage: www.elsevier.com/locate/jpowsour

Designing high-performance quasi-symmetrical solid oxide cells with a facile chemical modification strategy for $Sr_2Fe_{2-x}W_xO_{6-\delta}$ ferrites electrodes with *in situ* exsolution of nanoparticles

Kun Zheng [a,b,*], Jakub Lach [a], Paweł Czaja [c], Michał Gogacz [a], Patryk Czach [a], Agnieszka Brzoza-Kos [a], Piotr Winiarz [a], Jie Luo [d]

[a] AGH University of Krakow, Faculty of Energy and Fuels, Department of Hydrogen Energy, al. A. Mickiewicza 30, 30-059 Krakow, Poland
[b] AGH University of Krakow, AGH Centre of Energy, ul. Czarnowiejska 36, 30-054 Krakow, Poland
[c] Institute of Metallurgy and Materials Science, Polish Academy of Sciences, 25 Reymonta Str., 30-059, Kraków, Poland
[d] School of Materials Science and Hydrogen Energy, Foshan University, Foshan 528000, China

HIGHLIGHTS

- Tungsten doping significantly impacts physicochemical and electrochemical properties.
- $Sr_2Fe_{1.8}W_{0.2}O_{6-\delta}$ has the lowest Rp in air with 0.06 Ω cm^2 at 800 °C for 100 h.
- $Sr_2Fe_{1.6}W_{0.4}O_{6-\delta}$ shows the smallest Rp in 5% H_2 with 0.56 Ω cm^2 at 800 °C for 100 h.
- Symmetrical SOCs with 874 mW cm^{-2} power and 743 mA cm^{-2} current density at 1.5 V.
- *In situ* exsolved nanoparticles contribute to an excellent performance of cells.

GRAPHICAL ABSTRACT

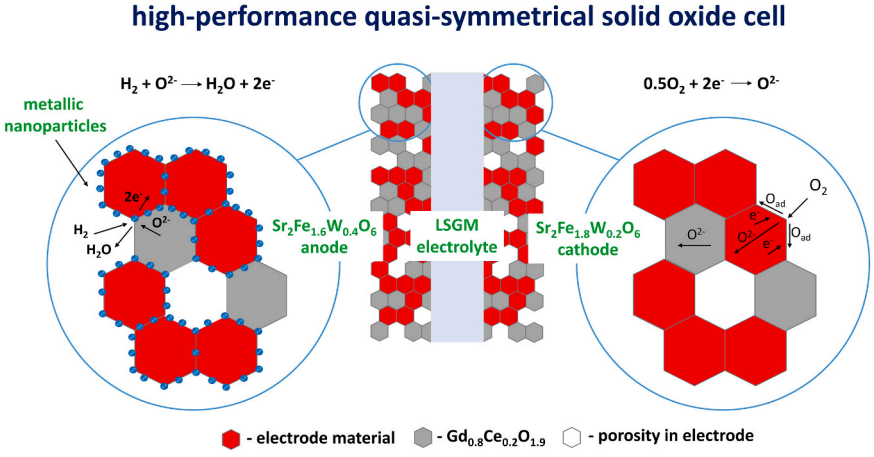

ARTICLE INFO

Keywords:
Symmetrical solid oxide fuel cell
Electrode materials
Perovskites
Nanoparticles
In situ exsolution

ABSTRACT

The chemical modification of perovskites is one of the most effective design strategies for electrode materials for solid oxide cells. In this work, the tungsten doping in $Sr_2Fe_{2-x}W_xO_{6-\delta}$ shows a significant impact on their physicochemical properties, and it leads to a substantial change of electrochemical properties in the air and reducing conditions, with $Sr_2Fe_{1.8}W_{0.2}O_{6-\delta}$ (R_p = 0.06 Ω cm^2 at 800 °C stable for 100 h in air) and $Sr_2Fe_{1.6}W_{0.4}O_{6-\delta}$ (Rp = 0.56 Ω cm^2 at 800 °C over 100 h in 5 vol% H_2/Ar) being the best air and fuel electrode candidates, respectively. We have proposed an attractive design of high-performance quasi-symmetrical solid oxide cells with 80%$Sr_2Fe_{1.8}W_{0.2}O_{6-\delta}$+20%GDC | LSGM | 80%$Sr_2Fe_{1.6}W_{0.4}O_{6-\delta}$+20%GDC, demonstrating excellent power outputs (874 mW cm^{-2} at 850 °C in wet H_2) and good current density of 743 mA cm^{-2} at 1.5 V in

* Corresponding author. AGH University of Krakow, Faculty of Energy and Fuels, Department of Hydrogen Energy, al. A. Mickiewicza 30, 30-059 Krakow, Poland.
E-mail address: zheng@agh.edu.pl (K. Zheng).

https://doi.org/10.1016/j.jpowsour.2023.233707
Received 13 August 2023; Received in revised form 21 September 2023; Accepted 2 October 2023

electrolysis mode at 750 °C. A good performance of 451 mW cm^{-2} was also recorded in wet CH_4 at 800 °C. The *in situ* exsolved metallic iron nanoparticles decorated on the $Sr_2Fe_{1.6}W_{0.4}O_{6-\delta}$ anode contribute to the excellent electrochemical performance of cells. This study provides a successful scenario for designing high-performance symmetrical solid oxide cells with a facile chemical modification strategy for ferrites electrodes with *in situ* exsolution of nanoparticles.

1. Introduction

The development of symmetrical Solid Oxide Cells (SOCs) with the same anode and cathode materials is of particular interest due to their various advantages, especially for the application in decentralized energy storage and conversion systems [1–7]. Depending on the actual energy demand, the symmetrical SOC can operate in a fuel cell or electrolysis mode. In the event of low electricity consumption, excess electrical energy can be stored in the fuel by electrolysis mode. Electrical energy and heat can be generated in the reverse mode of operation by utilizing the chemical energy of the fuel. The assembly of both anode and cathode electrodes in this type of SOCs uses the same material, which greatly simplifies the cell manufacturing procedure. By reducing the cell components in such a symmetric SOC configuration, problems of thermomechanical and chemical compatibility between the electrodes and the electrolyte can be minimized [8–10]. In addition, the carbon deposition and sulfur poisoning issues related to the use of cheaper and available fuels, such as methane, and natural gas, can be solved by a facile gas switching between the cathode and anode [1–4]. Recently, the configuration of quasi-symmetrical solid oxide fuel cell was also proposed to further improve the electrochemical performance of symmetrical cells, which optimally combines two different electrode materials for symmetrical cells as the anode and cathode simultaneously [11,12]. The application of mixed ionic-electronic conductors (MIEC) in the SOC electrode is considered to be highly beneficial, allowing for the electrode reaction to occur on the whole surface of the electrode, therefore, significantly enhancing the electrochemical performance [1–3,13–15]. Many new materials have been investigated and evaluated as electrode materials for symmetrical SOCs [1–7,16,19]. The requirements for electrode materials in symmetrical SOCs are strict, and they must meet all the criteria that apply to both anode and cathode materials at the same time. Among the proposed electrode materials, single-phase $SrFeO_{3-\delta}$-based perovskites with mixed ionic-electronic conductivity are particularly attractive because of their good electrical conductivities and capability to introduce oxygen vacancies, as well as high oxygen diffusion kinetics [5,20–22]. Symmetrical SOCs with Ti-doped $SrFeO_3$ electrodes and $La_{0.9}Sr_{0.1}Ga_{0.8}Mg_{0.2}O_{3-\delta}$ electrolyte exhibit high performance at relatively low temperatures (700 mW cm^{-2} at 800 °C) [7]. Studies on $SrFe_{0.75}M_{0.25}O_{3-\delta}$ (M = Ti, Zr, V, Nb, Cr, Mo, W) by Fernández-Ropero et al. suggested the potential application of these materials as electrode materials for symmetrical SOCs [23]. Fe- and Mo-containing $Sr_{2-x}Ba_xMMoO_6$ (M = Mg, Mn, Fe, Co, Ni) double perovskites [1,2,17,24] have been systematically investigated and show interesting physicochemical and electrochemical properties. Furthermore, $Sr_{1-x}Ba_xFe_{0.75}W_{0.25}O_{3-\delta}$ [16,23], $SrFe_{0.75}Mo_{0.25}O_{3-\delta}$ [17,18,25] and $SrFe_{0.5}Mn_{0.25}Mo_{0.25}O_{3-\delta}$ [17] perovskites show redox stability and have been evaluated as novel electrode materials for symmetrical SOCs fueled by methane or CO. Interestingly, symmetrical SOC cell with classical cathode material $La_{0.6}Sr_{0.4}Co_{0.2}Fe_{0.8}O_3$ as electrode material has also been reported to show good stability for over 100 h at 500 °C [19]. The high catalytic activity of $La_{0.6}Sr_{0.4}Co_{0.2}Fe_{0.8}O_3$ for CH_4 oxidation and good carbon deposition tolerance of symmetrical cells with such electrode material was demonstrated, but $La_{0.6}Sr_{0.4}Co_{0.2}Fe_{0.8}O_3$ shows instability in reducing conditions at high temperatures [26]. The redox stability of the electrodes for symmetrical SOCs is of utmost importance, especially after successive oxidizing/reducing cycles of operation. The phase transition of electrode materials at moderate temperatures is not favorable for the application, which may cause a delamination problem due to the mismatched thermal expansion coefficients between the electrodes and the electrolyte. $SrFeO_3$ can be possibly doped at B-site with different transition metals, such as Ti^{4+}, Si^{4+}, Zr^{4+}, Mo^{6+} and W^{6+}, which show improved redox stability in a wide range of temperatures and oxygen partial pressures [7,23,27–29].

This work applied a facile chemical modification strategy to develop cobalt-free $Sr_2Fe_{2-x}W_xO_{6-\delta}$ (x = 0.1 to 1.0) ferrites as potential redox−stable electrode materials for SOCs. The doping limit of tungsten has been determined. Physicochemical properties concerning the crystal structure and structure properties in function of temperature, thermal expansion properties, and oxygen nonstoichiometry of $Sr_2Fe_{2-x}W_xO_{6-\delta}$ oxides were thoroughly investigated. The studies of redox stability in reducing conditions and chemical compatibility of investigated perovskites towards typical electrolytes were also performed. High-performance quasi-Symmetrical Solid Oxide Cells were fabricated based on the selected electrode materials with *in situ* exsolved nanoparticles.

2. Experimental

2.1. The synthesis of $Sr_2Fe_{2-x}W_xO_{6-\delta}$ samples

$Sr_2Fe_{2-x}W_xO_{6-\delta}$ (x = from 0.1 to 1.0) compounds were synthesized by a high-temperature solid state reaction technique. Stoichiometric amounts of $SrCO_3$, Fe_2O_3, and WO_3 (all with ≥99.9% purity) initial chemicals were used and milled in a high-efficiency Spex Sample-Prep 8000 M planetary ball mill (in zirconia vials). After milling, the well-mixed powders were pressed into pellets and sintered for 10 h in air at 1200 °C for $Sr_2Fe_{2-x}W_xO_{6-\delta}$ (x = from 0.1 to 0.5), while in the case of $Sr_2Fe_{2-x}W_xO_{6-\delta}$ with higher content of tungsten (x = from 0.6 to 1) the synthesis condition of 1100 °C with 10 h firing in 5 vol% H_2 in argon was applied. In addition, the preparation of $Sr_2Fe_{2-x}W_xO_{6-\delta}$ (x ≥ 1.1) was also tried in 5 vol% H_2 in argon to determine the maximum doping level of tungsten in $Sr_2Fe_{2-x}W_xO_{6-\delta}$.

2.2. Characterization of physicochemical properties and redox stability of $Sr_2Fe_{2-x}W_xO_{6-\delta}$

The XRD data of the synthesized compounds $Sr_2Fe_{2-x}W_xO_{6-\delta}$ at room temperature (RT) were collected using Panalytical Empyrean diffractometer in the 10−110 deg range with CuKα radiation. The diffraction data were refined with the Rietveld method using the GSAS/EXPGUI set of software [30,31]. High temperature XRD measurements for $Sr_2Fe_{2-x}W_xO_{6-\delta}$ were performed on Panalytical Empyrean apparatus equipped with Anton Paar HTK 1200 N oven−chamber. The high temperature XRD data with refinements allowed for the calculation of thermal expansion coefficients (TEC). The Scanning Electron Microscopy (SEM) studies were performed using FEI Nova NanoSEM 200 apparatus on powders obtained after crushing and grinding of "as-synthesized" pellets. Thermal expansion studies were also conducted for the studied materials in the air up to 850 °C on Linseis L75 Platinum Series dilatometer.

Thermogravimetric (TG) measurements were performed on TA Instruments Q5000IR apparatus in RT−850 °C range in artificial air up to 850 °C with a heating rate of 2°·min^{-1}. For TG-based calculations, the buoyancy effect was appropriately considered. The total electrical conductivity of the studied samples was measured by a four-probe DC method for evaluation of the electrical conductivity (σ). Studies were

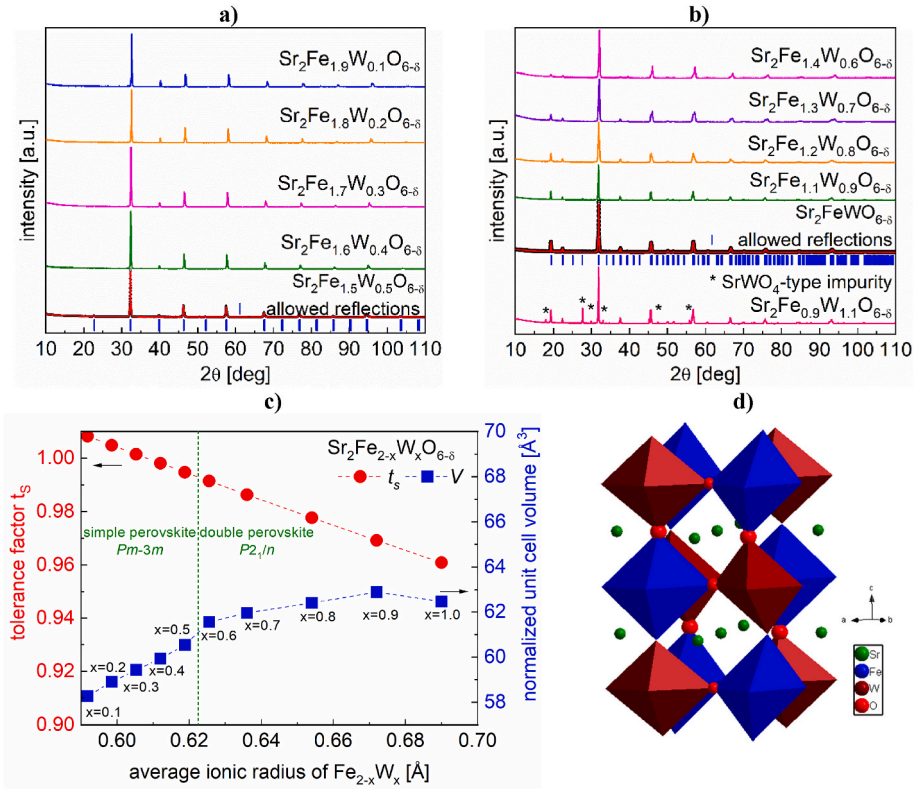

Fig. 1. (a) XRD patterns recorded for $Sr_2Fe_{2-x}W_xO_{6-\delta}$ (x = 0.1−0.5) synthesized in air, (b) $Sr_2Fe_{2-x}W_xO_{6-\delta}$ (x = 0.6−1) synthesized in 5 vol% H_2/argon, (c) Normalized unit cell volume and tolerance factor t_s for $Sr_2Fe_{2-x}W_xO_{6-\delta}$ (x = 0.1 to 1.0) perovskites as a function of ionic radius of $Fe_{2-x}W_x$. Error values are smaller than the visible points, (d) Visualization of the crystal structure of $Sr_2FeWO_{6-\delta}$ double perovskite.

done on dense samples with cuboid shapes (approx. 3 × 4 × 10 mm). The effect of the porosity of the sinters was taken into account, with an appropriate correction taken from Bruggeman's effective medium approximation [32].

The chemical stability and compatibility between electrode materials and the electrolyte is very essential for long-term stable cell operation. The chemical stability of the oxides under reducing conditions was evaluated by annealing the electrode materials under a reducing atmosphere of 5 vol% H_2/Ar at 800 °C for 24 h. After the annealing, consecutive XRD measurements were performed. Chemical compatibility studies of $Sr_2Fe_{2-x}W_xO_{6-\delta}$ (x = 0.1, 0.2, 0.3, 0.4 and 0.5, SFW) oxides towards typical solid electrolytes: GDC ($Ce_{0.8}Gd_{0.2}O_{1.9}$), LSGM ($La_{0.8}Sr_{0.2}Ga_{0.8}Mg_{0.2}O_{3-d}$) and 8YSZ (8 mol% yttria−stabilized zirconia) were evaluated by analyzing XRD data gathered for the respective electrode material and the electrolyte powder mixtures (50:50 wt%), which were fired at 900 °C and 1000 °C in air for 2 h, respectively. In addition, the chemical stability measurements were also conducted under reducing conditions (in 5 vol% H_2 in argon) at 850 °C for 10 h. The long-term chemical stability investigations were conducted at 800 °C for 100 h in air.

2.3. Construction and measurements of SFW-based symmetrical cells and LSGM-supported SOC

Dense LSGM electrolyte pellets (>98%) were fabricated by sintering in the air at 1450 °C for 8 h of pellets pressed (ca. 100 MPa uniaxial pressure) from well-ground LSGM powder with 1 wt% of poly(-vinyl butyral-co-vinyl alcohol-co-vinyl acetate) additive. For the assembly of LSGM-supported symmetrical SFW | LSGM | SFW cells and full cells, the LSGM electrolyte was polished down to the thickness of ca. 300 μm (using Struers Labopol-30 with MD-Piano 220 diamond polishing plate). Before the preparation of the SFW electrode slurry, the powder was pre-grounded in a mortar for 15 min. The electrode slurry was prepared by mixing the pre-ground SFW powder with an organic binder (terpineol-based 311,237 ink, FuelCellMaterials) and starch (pore former) in a weight ratio of 2:1:0.1. The prepared electrode paste was screen printed on the LSGM support with 2 layers on each side. The electrode layer of the symmetrical cells was sintered at 900 °C for 2 h. The silver paste (FuelCellMaterials) was painted by a proper brush in a form of a mesh pattern on both electrodes and Ag silver was used as the current collector, fired at 700 °C for 30 min. The working area of the electrodes was ca. 0.25 cm^2. Constructed symmetrical cells were studied to determine the electrode polarizations between 600 and 900 °C in air and 5 vol% H_2/Ar, respectively.

Quasi-symmetrical cells $Sr_2Fe_{1.8}W_{0.2}O_{6-\delta}$ | LSGM | $Sr_2Fe_{1.6}W_{0.4}O_{6-\delta}$ were fabricated with the same above-given fabrication technique and fired at various sintering temperatures (in the 850−1000 °C range in the air) to obtain the optimum sintering condition of quasi-symmetrical cells. For quasi-symmetrical cells with composite electrodes, cells with the configuration of 80%$Sr_2Fe_{1.8}W_{0.2}O_{6-\delta}$+20%GDC | LSGM (300 μm) | 80%$Sr_2Fe_{1.6}W_{0.4}O_{6-\delta}$+20%GDC were fired at 900 °C for 2 h.

The electrochemical performance of the constructed cells was studied using Solartron SI 1287 electrochemical interface and Solartron 1252A frequency response analyzer. Impedance spectroscopy was performed under open-circuit conditions in the 0.1 Hz–1 MHz range with a perturbation amplitude of 25 mV. Ohmic resistance R_{ohm} and the total interfacial polarization resistance with anode and cathode contributions ($R_p = R_a + R_c$) were refined corresponding to the equivalent circuit of $L-R_{ohm}-(RQ)_{HF}-(RQ)_{LF}$, where L represents inductance, R resistance, Q capacitive constant phase element, HF high-frequency contributions, and LF low-frequency contributions, respectively.

After cell measurements, the post-mortem examination of the anode with *in situ* exsolution of nanoparticles was conducted using ThermoScientific Titan Themis x-FEG Cs Corrected 200 kV scanning transmission electron microscopy. Thin foils were cut from the anode for transmission electron microscopy (TEM) studies employing the focused

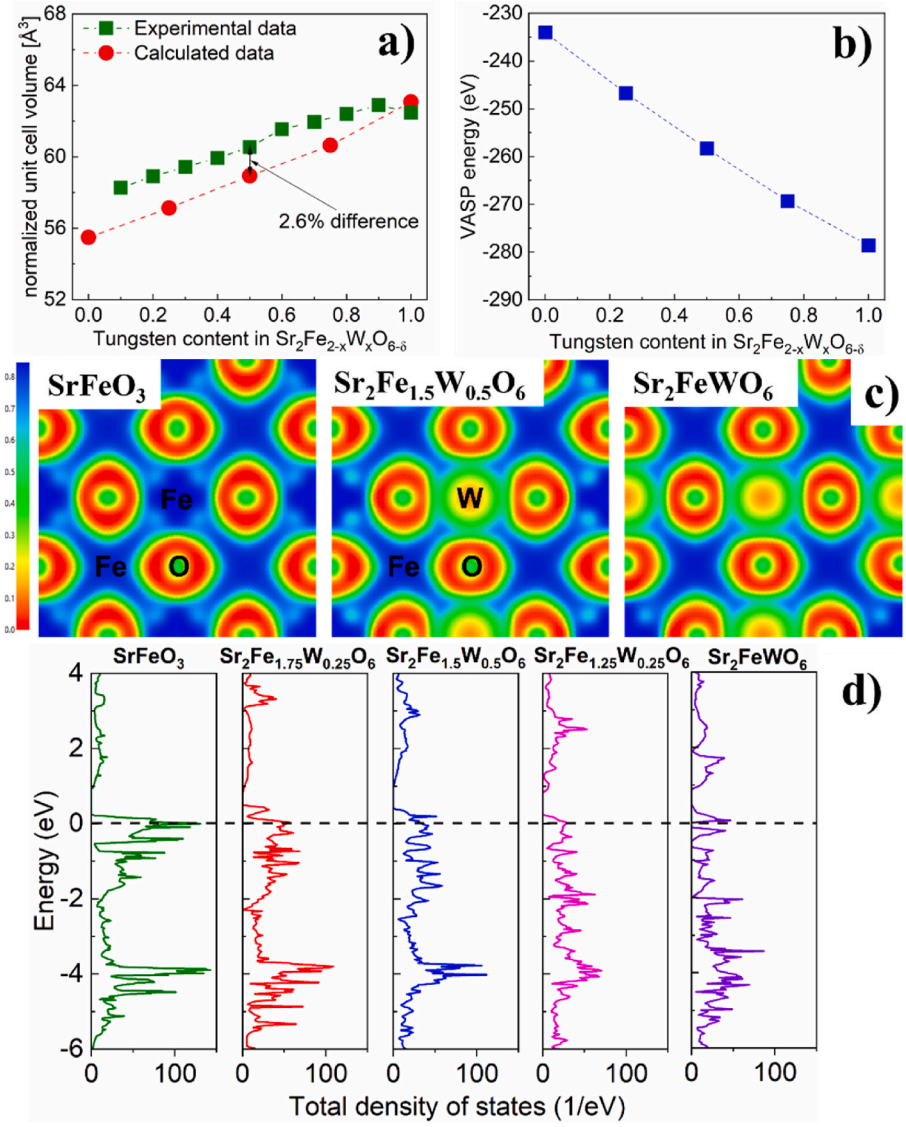

Fig. 2. (a) Calculated data and experimental normalized unit cell volumes for $Sr_2Fe_{2-x}W_xO_{6-\delta}$, (b) The calculated total energies, (c) The electron localization functions (red = 0%, dark blue = 80%) of $Sr_2Fe_{2-x}W_xO_{6-\delta}$ and (d) the total density of states of $Sr_2Fe_{2-x}W_xO_{6-\delta}$. (For interpretation of the references to colour in this figure legend, the reader is referred to the Web version of this article.)

ion beam technique (FIB), using ThermoScientific SCIOS II Dual Beam.

2.4. Quantum mechanical calculations

For ab initio theoretical calculations, Density Functional Theory (DFT) was applied utilizing Vienna Ab initio Simulation Package and MedeA external software. The generalized gradient approximation for the exchange−correlation energy according to Perdew, Burke, and Ernzerhof was used for all calculations [33]. For cell optimizations, an increased plane−wave cutoff equal to 520 eV was used. Based on the literature, the DFT + U method was employed, where U was equal to 4.3 eV and 4.0 eV respectively for Fe and W 3d electrons [34–36]. The structural optimizations, total energy calculations, density of states (DOS), and electron localization function were performed on 2 × 2 × 2 constructed supercells, giving the chemical formula $Sr_8Fe_{8-y}W_yO_{24-\delta}$. Using the blocked Davidson algorithm, the convergence energy was set to 1.0×10^{-5} eV per atom, and 0.02 eV/Å for force. The electron localization function was calculated and shown for the (001) plane, regarding the Fe atom as a central one, located at ½ ½ ½ of the considered supercell. For DOS analysis, O 2p, Sr 3d, Fe 3d, and W 3d electrons were considered, giving the highest contribution to total DOS.

3. Results and discussion

3.1. Crystal structure and the doping level of tungsten in $Sr_2Fe_{2-x}W_xO_{6-\delta}$

The XRD profile of obtained single phase $Sr_2Fe_{2-x}W_xO_{6-\delta}$ (x = 0.1 to 1.0) powder is presented in Fig. 1a and b, and the Rietveld refinement results are shown in Table S1. Strontium ferrite $SrFeO_{3-\delta}$ based on the oxygen content possesses different crystal structures: conventional *Pm*-3*m* space group and orthorhombic *Cmmm* space group [37]. The tungsten doping (with x = 0.1 to 0.5) in strontium ferrite stabilizes the crystal structure of $Sr_2Fe_{2-x}W_xO_{6-\delta}$ to be cubic crystal structure *Pm*-3*m* (simple perovskite), see Fig. 1a. This agrees with the literature data that $Sr_2Fe_{1.8}W_{0.2}O_{3-\delta}$ [32], $Sr_2Fe_{1.6}W_{0.4}O_{3-\delta}$ [38] and $Sr_2Fe_{1.5}W_{0.5}O_{6-\delta}$ [16, 23] show simple perovskite structure with *Pm*-3*m* space group. While T. Su et al. reported that $Sr_2Fe_{1.6}W_{0.4}O_{3-\delta}$ [32] possesses a tetragonal crystal structure with an *I*4/*m* space group, which may be related to the synthesis condition. $Sr_2Fe_{2-x}W_xO_{6-\delta}$ oxides with a low content of tungsten (x = 0.1 to 0.5) can be easily synthesized in air, see Fig. 1a. It is

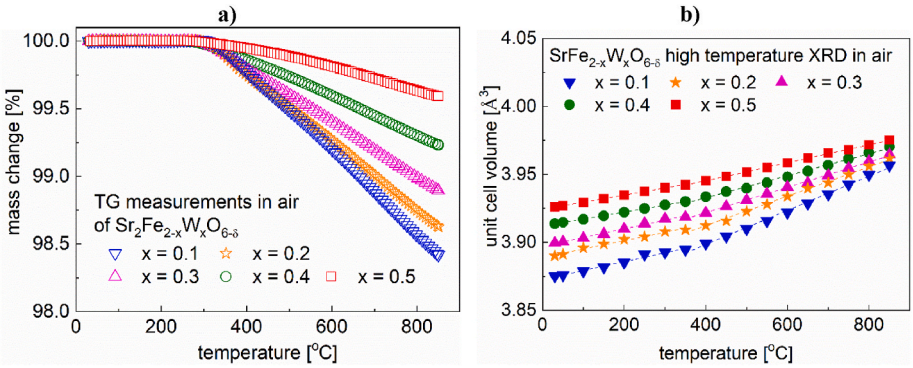

Fig. 3. (a) Oxygen content change of $Sr_2Fe_{2-x}W_xO_{6-\delta}$ (x = 0.1−0.5) in air, (b) XRD in-situ measurements of $Sr_2Fe_{2-x}W_xO_{6-\delta}$ (x = 0.1−0.5) from 30 to 900 °C in air.

reported that the valence of iron in $SrFeO_{3-\delta}$ perovskite oxides usually shows a mixed state including Fe^{3+} and Fe^{4+} [38]. The XPS studies of $Sr_2Fe_{1.6}W_{0.4}O_{6-\delta}$ (simple perovskite $SrFe_{0.8}W_{0.2}O_{3-\delta}$) showed the valence state of Fe^{4+}/Fe^{3+} in tungsten doped strontium ferrite [38,39]. Moreover, the valence state of W stabilizes at +6 in $Sr_2Fe_{1.6}W_{0.4}O_{6-\delta}$ oxide, even after the reduction in 5% H_2 at 850 °C [39]. Based on the charge neutrality requirement in $Sr_2Fe_{2-x}W_xO_{6-\delta}$ (x = 0.1 to 0.5) materials, the iron substitution with tungsten should decrease the content of Fe^{4+} and simultaneously increase the concentration of Fe^{3+}. The size of Fe^{4+} ($r_{Fe4+} = 0.585$ Å) is smaller than the size of Fe^{3+} ($r_{Fe3+} = 0.645$ Å) and W^{6+} ($r_{W6+} = 0.6$ Å) cations. Therefore, the unit cell parameters of $Sr_2Fe_{2-x}W_xO_{6-\delta}$ (x = 0.1 to 0.5) increase with the increasing tungsten content, as observed in Fig. 1c.

The further increase of tungsten content in $Sr_2Fe_{2-x}W_xO_{6-\delta}$ (x ≥ 0.6) significantly changes the crystal structure of materials (Fig. 1b). The appearance of peaks around 2theta = 19.4 and 22.4° confirms the different crystal structure of materials with high tungsten content (x ≥ 0.6), which can only be synthesized in the reducing condition (5 vol% H_2 in argon). The maximum doping level of tungsten in $Sr_2Fe_{2-x}W_xO_{6-\delta}$ is confirmed to be limited to x = 1.0, and the further increase of tungsten in $Sr_2Fe_{2-x}W_xO_{6-\delta}$ (x ≥ 1.1) leads to the appearance of an evident presence of $SrWO_4$-type impurity (see Fig. 1b). As Sr_2FeWO_6 has been identified with $P2_1/n$ space group (B-site cations ordering double perovskite) by the neutron powder diffraction studies [40], in this study the $P2_1/n$ space group has been applied to refine the XRD data for all $Sr_2Fe_{2-x}W_xO_{6-\delta}$ (x = 0.6 to 1.0) materials. The B-site rock salt-type ordered double perovskite structure with $P2_1/n$ space group is visualized in Fig. 1d for Sr_2FeWO_6.

As $Sr_2Fe_{2-x}W_xO_{6-\delta}$ (x = 0.6 to 1.0) double perovskites were synthesized in the reducing condition, the valences of Fe^{3+} and Fe^{2+} should be dominant in those materials containing high content of tungsten. The increase of tungsten in $Sr_2Fe_{2-x}W_xO_{6-\delta}$ (x = 0.6 to 1.0) oxides causes the replacement of Fe^{3+} ($r_{Fe3+} = 0.645$ Å) with Fe^{2+} ($r_{Fe2+} = 0.78$ Å), which increases the unit cell volume of materials (see Table S1 and Fig. 1c). However, the substation of iron (Fe^{2+} with 0.78 Å) with tungsten (W^{6+} with 0.6 Å) can also decrease the unit cell volume of $Sr_2Fe_{2-x}W_xO_{6-\delta}$ materials. The unit cell volume decrease has been observed when tungsten doping increases from $Sr_2Fe_{1.1}W_{0.9}O_6$ to Sr_2FeWO_6 oxide (see Fig. 1c). The presence of Fe^{2+} (high spin, $S = 2$) in Sr_2FeWO_6 has been confirmed by H. Kawanaka et al. [41]. It has also been found that in Sr_2FeWO_6, the values of valences for iron and tungsten are close to Fe^{2+} and W^{6+}, determined by three different techniques (neutron powder diffraction, X-ray photoemission spectroscopy, and X-ray absorption spectroscopy) [40]. Interestingly, $SrWO_4$ cannot be reduced to $SrWO_3$ even at high temperatures [42], indicating that the reduction of W^{6+} to low oxygen states is very difficult. Therefore, the maximum doping level in $Sr_2Fe_{2-x}W_xO_{6-\delta}$ ferrites is limited to x = 1.0 ($Sr_2Fe^{2+}W^{6+}O_6$), and a further increase of tungsten content (such as x = 1.1) causes the appearance of $SrWO_4$ impurity (see Fig. 1b) which can be primarily described by the following equation: $Sr_2Fe_{0.9}W_{1.1}O_{6-\delta} \rightarrow 0.9Sr_2FeWO_{6-\delta} + 0.2SrWO_4$.

The incorporation of tungsten cation into the crystal structure of strontium ferrite induces strain in $Sr_2Fe_{2-x}W_xO_{6-\delta}$ perovskites which has to be distributed. Quantifying the magnitude of this strain as a function of tungsten content in $Sr_2Fe_{2-x}W_xO_{6-\delta}$ can be evaluated based upon the relative ratio of W^{6+} to the incumbent compounds. The tolerance factor t_s of $Sr_2Fe_{2-x}W_xO_{6-\delta}$ perovskites was calculated with the following equation: $t_s = \frac{[r_{Sr}+r_O]}{\sqrt{2}[x\bullet r_W+(1-x)r_{Fe}+r_O]}$, where x refers to the mole percent of tungsten present at B site, and r denotes the ionic radius [24,43,44]. By tungsten doping, the tolerance factor t_s calculated on a basis of Goldschmidt's equation, gradually decreases (Fig. 1c), which indicates the increase in strain and causes the crystal structure of materials deviating from the regular cubic structure. This tendency agrees with the recorded crystal structure change from regular $Pm\text{-}3m$ to $P2_1/n$ when the tungsten content increases to x ≥ 0.6 (Fig. 1c).

As can be seen from Fig. 2a, the calculated normalized unit cell volume agrees well with the experimental data, suggesting that geometry optimization is correct. Comparing the trend lines, the difference doesn't exceed 3% of the volume change. The total energy of the $Sr_2Fe_{2-x}W_xO_{6-\delta}$ systems (Fig. 2b) decreases with the increased content of tungsten. The more negative values suggest a more stable structure of high tungsten content materials, which agrees with the experimental data (see the section on stability studies), indicating a more stable structure in reducing atmospheres for the tungsten-rich compounds. The electron localization function (Fig. 2c) was shown for the (001) plane in the unit cell. The left image shows delocalized electrons for the undoped $SrFeO_3$ sample indicating the highest probability of finding electrons in the vicinity of iron atoms. The lowest probability is geometrically located near oxygen atoms and strontium atoms (not visible here for the latter). In the case where iron is substituted by tungsten, one can see a decrease of electron localization probability, not only in the nearest area but also light blue spots visible near the oxygens located {001} faces of the unit cell. In the right image, where Fe and W have the same occupancy, the probability of finding the electron is the lowest. This corresponds with the tendency of total conductivity data change for $Sr_2Fe_{2-x}W_xO_{6-\delta}$ recorded in Fig. 4, where the total conductivity is lowered with the increasing tungsten content. Also, the DOS calculations indicate that the total amount of states decreases for the materials with a greater amount of tungsten. The highest amount of DOS is noticed for the undoped sample (see Fig. 2d). Interestingly, there is a small band gap for $Sr_2FeWO_{6-\delta}$, which equals $E_g = 0.133$ eV indicating the semiconducting behavior of this system, contrary to other ones. One has to notice that the DOS calculations are performed for the absolute temperature of 0 K, which could deviate from the actual data measured from the elevated temperatures. However, the tungsten doping effect in $Sr_2Fe_{2-x}W_xO_{6-\delta}$ systems on the conductivity properties evaluated by the theoretical calculations is confirmed by the conductivity studies in Fig. 4a.

In the following, $Sr_2Fe_{2-x}W_xO_{6-\delta}$ (x = 0.1 to 0.5) materials

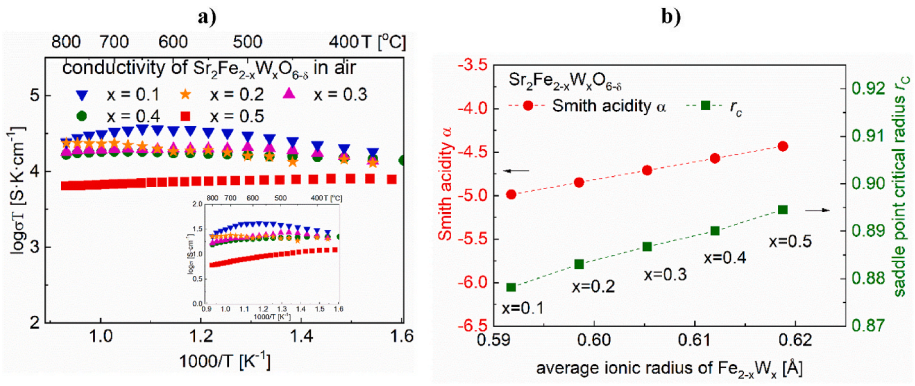

Fig. 4. (a) Electrical conductivity of $Sr_2Fe_{2-x}W_xO_{6-\delta}$ (x = 0.1−0.5) samples in air, (b) Smith acidity and saddle point critical radius of $Sr_2Fe_{2-x}W_xO_{6-\delta}$.

Table 1
Oxygen content change of $Sr_2Fe_{2-x}W_xO_{6-\delta}$ (x = 0.1, 0.2, 0.3, 0.4, 0.5) oxides between 30 °C and 850 °C in air.

$Sr_2Fe_{2-x}W_xO_{6-\delta}$	x = 0.1	x = 0.2	x = 0.3	x = 0.4	x = 0.5
oxygen content change [mol·mol^{-1}]	**0.20**	**0.18**	**0.15**	**0.11**	**0.06**

Table 2
Thermal expansion coefficients of $Sr_2Fe_{2-x}W_xO_{6-\delta}$ (x = 0.1, 0.2, 0.3, 0.4, 0.5) oxides from dilatometer measurements and high temperature XRD studies in air.

	$Sr_2Fe_{2-x}W_xO_{6-\delta}$	x = 0.1	x = 0.2	x = 0.3	x = 0.4	x = 0.5
TEC [10^{-6} K^{-1}]	dilatometer measurements 30−850 °C	24.5	21.4	20.7	17.3	15.3
	HT-XRD (30–350 °C)	16.9	15.8	16.4	13.1	13.3
	HT-XRD (350−850 °C)	32.2	27.6	23.7	20.6	16.8

synthesized in the air with possible high conductivities, were selected for further characterizations and evaluated as electrode (both anode and cathode) materials for symmetrical SOCs.

3.2. Oxygen nonstoichiometry and thermal expansion properties

The mass change related to the oxygen content change in $Sr_2Fe_{2-x}W_xO_{6-\delta}$ (x = 0.1 to 0.5) oxides was recorded in the air from 30 °C to 850 °C, as shown in Fig. 3a. In all measured oxides, the mass change/reduction starts above 300 °C, indicating the creation of oxygen vacancies, which favours the oxygen ion transport in the materials. The oxygen content change is strictly only related to the reduction of Fe^{4+} to Fe^{3+} in materials, due to the stable W^{6+} state (even in the reducing condition) [40]. Therefore, it can be expected that the increasing content of tungsten (substituting the iron) in $Sr_2Fe_{2-x}W_xO_{6-\delta}$ (x = 0.1−0.5) materials reduces the oxygen nonstoichiometry δ, as the amount of $Fe^{4+} - Fe^{3+}$ reduction pair decreases. The formation of oxygen vacancies and the reduction of Fe^{4+} to Fe^{3+} can be described by the following equation with Kröger−Vink notation: $2Fe^{4+} + O_O^X \rightarrow V_O^{\bullet\bullet} + 2Fe^{3+} + \frac{1}{2}O_2(g)$. The largest amount of calculated oxygen content change between 30 °C and 850 °C was recorded for $Sr_2Fe_{1.9}W_{0.1}O_{6-\delta}$ with 0.20 mol mol^{-1}, while $Sr_2Fe_{1.5}W_{0.5}O_{6-\delta}$ shows the least with 0.06 mol mol^{-1} (see Table 1). The in-situ XRD measurements of $Sr_2Fe_{2-x}W_xO_{6-\delta}$ (x = 0.1−0.5) compounds were conducted from 30 °C to 850 °C in the air (Fig. 3b), and as expected no phase transitions have been observed for all compounds. The normal increase of unit cell parameters (volumes) associated with the thermal expansion behavior was recorded for all investigated samples from 30 °C to around 350 °C. While for the high temperature range, a much more significant unit cell volume change was observed, due to the generation of oxygen vacancies in the materials, corresponding to the recorded mass reduction in TG measurements. The thermal expansion coefficient (TEC) can be calculated based on the high temperature XRD data. As can be observed in Table 2, the replacement of iron with tungsten in $Sr_2Fe_{2-x}W_xO_{6-\delta}$ (x = 0.1−0.5) decreases the TEC values, which is favorable for the construction of durable and stable electrode layers without the delamination issue. The chemical expansion (due to the oxygen release from the samples) above 350 °C in $Sr_2Fe_{2-x}W_xO_{6-\delta}$ contributes to larger TECs than the values recorded at the low temperature range (<350 °C). Dilatometry measurements have been conducted for all $Sr_2Fe_{2-x}W_xO_{6-\delta}$ (x = 0.1−0.5) samples (see Fig. S1) and the measured TEC values (in 15.3–24.5 × 10^{-6} K^{-1} range) are gathered in Table 2. A similar TEC value with 18.4 × 10^{-6} K^{-1} was recorded for $SrFe_{0.8}W_{0.2}O_{3-\delta}$ [39]. The conducted dilatometry measurements confirmed the positive doping effect of tungsten doping in $Sr_2Fe_{2-x}W_xO_{6-\delta}$ materials which was also observed in the high temperature XRD studies, and the increased content of tungsten decreases the TEC values. The evident contribution of the chemical expansion related to oxygen release from materials can be observed for all $Sr_2Fe_{2-x}W_xO_{6-\delta}$ compounds above 400 °C (Fig. S1). The largest TEC (24.5 × 10^{-6} K^{-1}) was recorded for $Sr_2Fe_{1.9}W_{0.1}O_{6-\delta}$, and the smallest TEC coefficient with 15.3 × 10^{-6} K^{-1} (in the 30−850 °C range) was recorded for $Sr_2Fe_{1.5}W_{0.5}O_{6-\delta}$. The tungsten doping reduces the volume change of $Sr_2Fe_{2-x}W_xO_{6-\delta}$ induced by the lattice oxygen loss, decreasing the TECs close to values of typical electrolytes, such as $La_{0.9}Sr_{0.1}Ga_{0.8}Mg_{0.2}O_{3-\delta}$ − 12.17 × 10^{-6} K^{-1}, $Zr_{0.85}Y_{0.15}O_{2-\delta}$ − 10.8 × 10^{-6} K^{-1} and $Ce_{0.8}Gd_{0.2}O_{2-\delta}$ − 12.5 × 10^{-6} K^{-1} [24,45].

3.3. Transport properties of $Sr_2Fe_{2-x}W_xO_{6-\delta}$ (x = 0.1−0.5) oxides

The collected electrical conductivity data of $Sr_2Fe_{2-x}W_xO_{6-\delta}$ (x = 0.1−0.5) oxides between 350 and 800 °C show the increased content of tungsten decreases the total electrical conductivity in air (Fig. 4a). $Sr_2Fe_{1.9}W_{0.1}O_{6-\delta}$ compound presents the highest conductivity among all studied materials, with the maximum peak value of 40.5 S cm^{-1} at 600 °C (see Table S2). The conductivity increase tendency with temperature, followed by a decrease above 600 °C, is related to the increase in oxygen vacancy concentration of predominant n-type conductive materials [23]. Similar phenomena have been recorded in other $SrFeO_3$-based materials [46]. In $Sr_2Fe_{1.9}W_{0.1}O_{6-\delta}$ sample, electrons are transmitted via Fe^{3+}−O^{2-}−Fe^{4+} network. Therefore, the release of lattice oxygen at high temperatures breaks the Fe^{3+}−O^{2-}−Fe^{4+} network, resulting in a decrease in electrical conductivities. The lowest conductivity value of $Sr_2Fe_{2-x}W_xO_{6-\delta}$ (x = 0.1−0.5) oxides was observed in $Sr_2Fe_{1.5}W_{0.5}O_{6-\delta}$ (6.0 S cm^{-1} at 800 °C). In general, the increasing tungsten content in $Sr_2Fe_{2-x}W_xO_{6-\delta}$ (x = 0.1−0.5) reduces the effective concentration of electronic charge carrier, thus leading to the decrease of electrical conductivity, which is consistent with the thermally

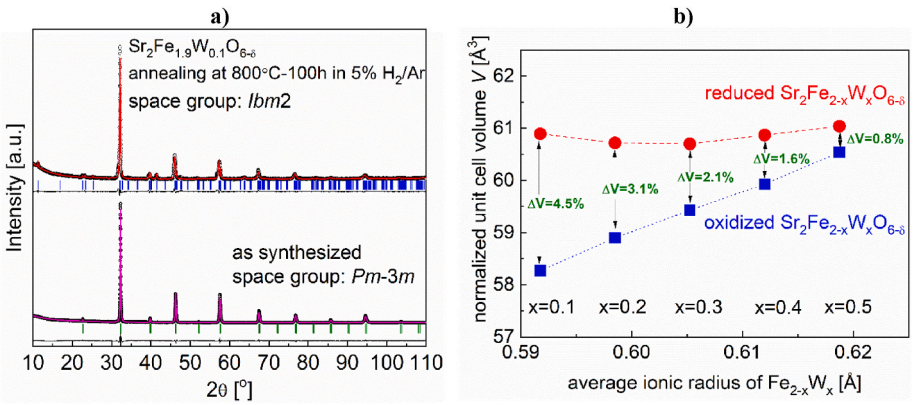

Fig. 5. (a) Exemplary XRD patterns of $Sr_2Fe_{1.9}W_{0.1}O_{6-\delta}$, (b) Normalized unit cell volume of reduced and oxidized $Sr_2Fe_{2-x}W_xO_{6-\delta}$ (x = 0.1−0.5) as a function of B-site cations ($Fe_{2-x}W_x$) ionic radius.

activated small polaron hopping mechanism [46].

The oxygen ion mobility is an influencing factor for the ionic conductivity of materials. In the perovskite lattice, the oxygen migration transports through the space of a triangle formed by two A site cations and one B site cation, the radius of which is defined as the saddle point critical radius r_c. The following equation is generally applied to evaluate the critical radius r_c [47]: $r_c = \frac{-r_A^2+\frac{3}{4}a^2-\sqrt{2}a\times r_B+r_B^2}{2r_A+\sqrt{2}a-2r_B}$, where r_A and r_B are the radii of A and B site cations in the perovskite, respectively, and a is the pseudo−cubic symmetry lattice constant. In general, the critical radius r_c in most perovskite structure does not exceed 1.0 Å, which is smaller than the oxygen ion radii (1.40 Å). Therefore, it leads to a required activation energy for the oxygen ion migration within the perovskite structure. The tungsten doping in $Sr_2Fe_{2-x}W_xO_{6-\delta}$ (x = 0.1−0.5) perovskites contributes to an increase of saddle point critical radius r_c (Fig. 4b), which shows a decrease of oxygen ion migration activation energy with the increase content of W, favoring the oxygen ion transport in materials.

It has been reported that the oxygen exchange kinetics are strongly linked with the calculated Smith acidity α of perovskite oxides with mixed conducting properties [48,49]. The expression of Smith acidity α for double perovskite oxides with the general formula $A_2B_{2-x}B'_xO_6$ is as follow: $\alpha_{A_2B_{2-x}B'_xO_6} = \frac{2\alpha_{AO}+(2-x)\alpha_{BO}+x\alpha_{B'O}}{4}$ [48]. The iron substitution with tungsten in $Sr_2Fe_{2-x}W_xO_{6-\delta}$ (x = 0.1−0.5) increases the Smith acidity value (Fig. 4b), which may indicate the decrease of oxygen exchange kinetics with the increase of tungsten content [48,49].

3.4. Chemical stability and compatibility of $Sr_2Fe_{2-x}W_xO_{6-\delta}$ (x = 0.1−0.5) with electrolytes

To evaluate the possible application of $Sr_2Fe_{2-x}W_xO_{6-\delta}$ (x = 0.1−0.5) oxides as anode materials for solid oxide fuel cells (SOFCs), the stability of $Sr_2Fe_{2-x}W_xO_{6-\delta}$ compounds was investigated in the reducing condition (5 vol% H_2 in argon) at 800 °C for 100 h. Exemplary XRD patterns with the Rietveld refinement of the reduced samples are

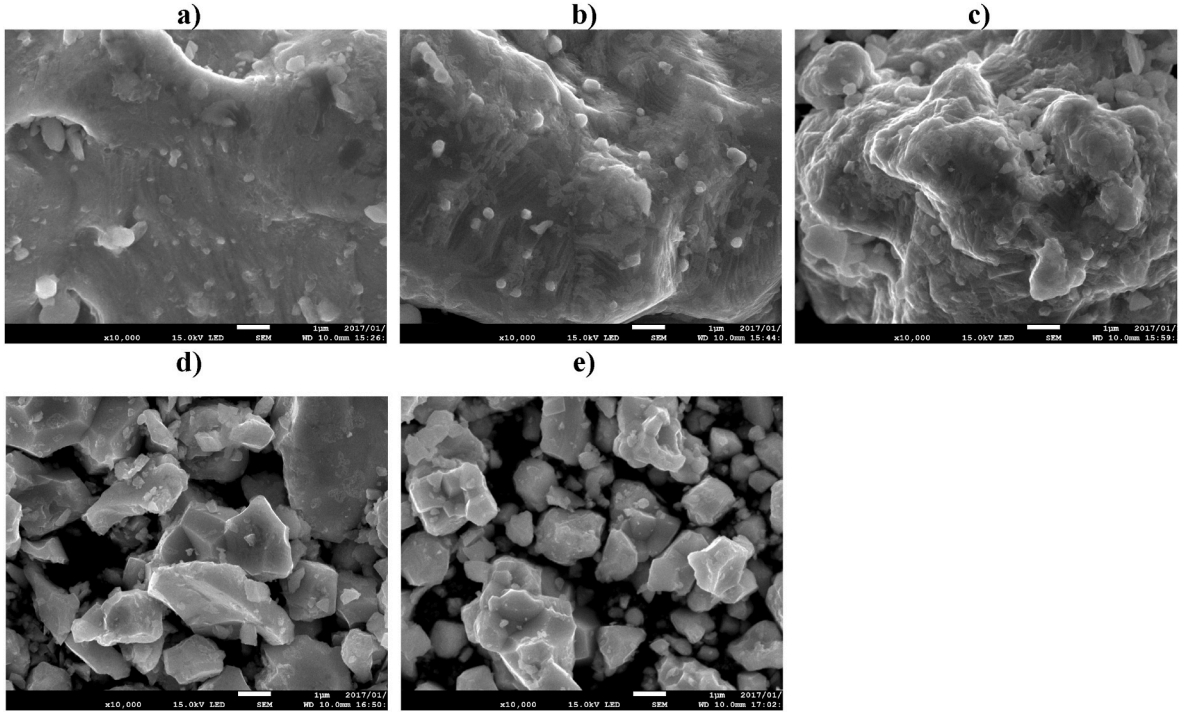

Fig. 6. SEM microphotograph of $Sr_2Fe_{2-x}W_xO_{6-\delta}$ with (a) x = 0.1, (b) x = 0.2, (c) x = 0.3, (d) x = 0.4, (e) x = 0.5 powders reduced at 800 °C for 100 h in 5 vol% H_2 in argon.

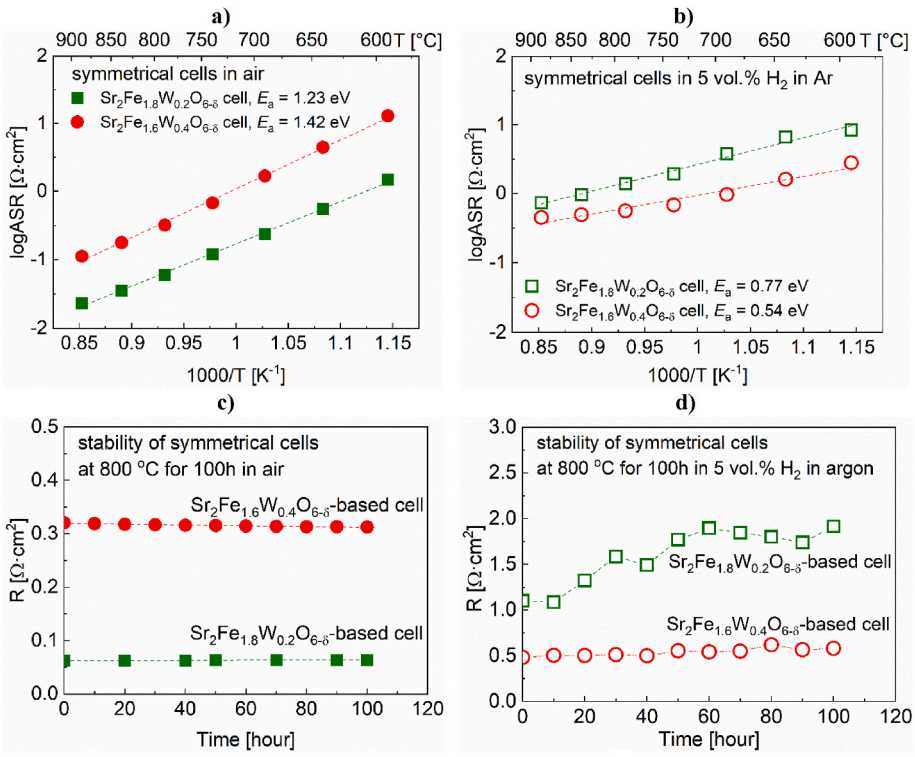

Fig. 7. Electrode polarization resistance dependence on temperature of $Sr_2Fe_{1.8}W_{0.2}O_{6-\delta}$ and $Sr_2Fe_{1.6}W_{0.4}O_{6-\delta}$ (data plotted in Arrhenius−type coordinates) together with activation energy values (a) in air and (b) in 5 vol% H_2 in argon, polarization resistance dependence on time at 800 °C for 100 h (c) in air and (d) in 5 vol% H_2 in argon.

presented in Fig. 5a, and all XRD patterns of $Sr_2Fe_{2-x}W_xO_{6-\delta}$ (x = 0.1−0.5) oxides after annealing in the reducing condition are presented in Fig. S2 in the supplement. The Rietveld refinement results of $Sr_2Fe_{2-x}W_xO_{6-\delta}$ (x = 0.1, 0.2, 0.3, 0.4 and 0.5) compounds reduced at 800 °C for 100 h in 5 vol% H_2 in argon are gathered in Table S3. As can be expected, the unit cell parameters of reduced $Sr_2Fe_{2-x}W_xO_{6-\delta}$ are much larger than oxidized counterparts, which is associated with the reduction of iron oxygen state ($r_{Fe4+} = 0.585$ Å, $r_{Fe3+} = 0.645$ Å, $r_{Fe2+} = 0.78$ Å). All $Sr_2Fe_{2-x}W_xO_{6-\delta}$ (x = 0.1−0.5) compounds remain stable after the reduction at 800 °C for 100 h in 5 vol% H_2 in argon, and no secondary phase has been detected by the XRD studies. Interestingly, the reduced $Sr_2Fe_{1.9}W_{0.1}O_{6-\delta}$ with the least content of tungsten (x = 0.1) shows a brownmillerite structure ($A_2B_2O_5$) with *Ibm*2 space group, which indicates the reduced compound possesses a large number of oxygen vacancies with a perovskite−related structure [50]. Other reduced oxides ($Sr_2Fe_{2-x}W_xO_{6-\delta}$ with x = 0.2−0.5) show the same simple perovskite structure (*Pm*-3*m*) as the oxidized ones.

The respective unit cell volume data for the reduced and oxidized $Sr_2Fe_{2-x}W_xO_{6-\delta}$ (x = 0.1−0.5) samples are presented in Fig. 5b. The relative change of unit cell volumes of $Sr_2Fe_{2-x}W_xO_{6-\delta}$, calculated as a difference between values for reduced and oxidized oxides and divided by values for the reduced counterparts, respectively, is also shown in Fig. 5b. It can be noted that the increasing content of tungsten in $Sr_2Fe_{2-x}W_xO_{6-\delta}$ decreases the relative volume change, which can be expected due to the decrease content of iron with changeable oxidation states. The relative unit cell volume change between reduced and oxidized $Sr_2Fe_{2-x}W_xO_{6-\delta}$ (x = 0.1−0.5) is between 4.5% and 0.8%, much lower than the NiO to Ni volume contraction of ~40% in the typical anode material for SOFCs [51], which favors the application of $Sr_2Fe_{2-x}W_xO_{6-\delta}$ (x = 0.1−0.5) oxides both in reducing and oxidizing conditions, such as electrode materials for symmetrical SOFCs.

The microstructure of reduced $Sr_2Fe_{2-x}W_xO_{6-\delta}$ (x = 0.1−0.5) powders has been investigated by SEM studies (see Fig. 6). SEM microphotographs of $Sr_2Fe_{2-x}W_xO_{6-\delta}$ (x = 0.1−0.5) with × 1000 resolution are presented Fig. S3. In general, $Sr_2Fe_{2-x}W_xO_{6-\delta}$ (x = 0.1−0.3) materials revealed very similar microstructure and well−sintered aggregates are present. The results indicate good sinterability of the powders. While $Sr_2Fe_{2-x}W_xO_{6-\delta}$ (x = 0.4−0.5) perovskites present much smaller particles. Exsolved nanoparticles can be detected on the surface of $Sr_2Fe_{2-x}W_xO_{6-\delta}$ (x = 0.1 and 0.2) samples, but for $Sr_2Fe_{2-x}W_xO_{6-\delta}$ (x = 0.3, 0.4 and 0.5) the presence of exsolved nanoparticles is not evident, indicating the increased content of tungsten enhancing the stability of materials in the reducing condition. As shown in work [39], W-containing $Sr_2Fe_{1.8}W_{0.2}O_{6-\delta}$ oxide can be reduced to $Sr_3Fe_2O_6$, metal Fe and Sr_2FeWO_6 in humidified hydrogen, while $Sr_2Fe_{1.6}W_{0.4}O_{6-\delta}$ still stays stable without a decomposition. Therefore, We believe that in a strong reducing condition (pure hydrogen) $Sr_2Fe_{1.9}W_{0.1}O_{6-\delta}$ and $Sr_2Fe_{1.8}W_{0.2}O_{6-\delta}$ compounds could be decomposed to $Sr_3Fe_2O_6$, iron and Sr_2FeWO_6, while $Sr_2Fe_{1.6}W_{0.4}O_{6-\delta}$ remains the primitive perovskite structure as We have confirmed it in the following studies. The exsolved nanoparticles from $Sr_2Fe_{2-x}W_xO_{6-\delta}$ samples were studied in detail in the section contributing to *in situ* exsolution of metallic nanoparticles. Of importance, as presented in a section devoted to electrochemical studies of selected $Sr_2Fe_{2-x}W_xO_{6-\delta}$ electrode materials, an additional milling has been applied for obtaining fine powder suitable for the sintering of electrodes.

The stability of electrode materials at working temperature and their compatibility with applied electrolytes are very crucial for the long stable performance of solid oxide cells. Therefore, the chemical stability and compatibility of $Sr_2Fe_{2-x}W_xO_{6-\delta}$ (x = 0.1−0.5) with mostly used electrolytes (GDC: $Ce_{0.8}Gd_{0.2}O_{1.9}$, LSGM: $La_{0.8}Sr_{0.2}Ga_{0.8}Mg_{0.2}O_{3-d}$, and 8YSZ: 8 mol% yttria-stabilized zirconia) have been investigated at 900 °C for 2 h and 1000 °C for 2 h (the sintering temperature of symmetric cells), respectively. As can be observed in Figs. S4, S5, S7, S8 and Tables S4, S5, S7, S8 in the supplement, $Sr_2Fe_{2-x}W_xO_{6-\delta}$ (x = 0.1, 0.2, 0.3, 0.4 and 0.5) compounds are compatible with GDC and LSGM ceramic electrolytes at 900 °C and 1000 °C, and no additional peaks related with the reaction between studied materials and electrolytes

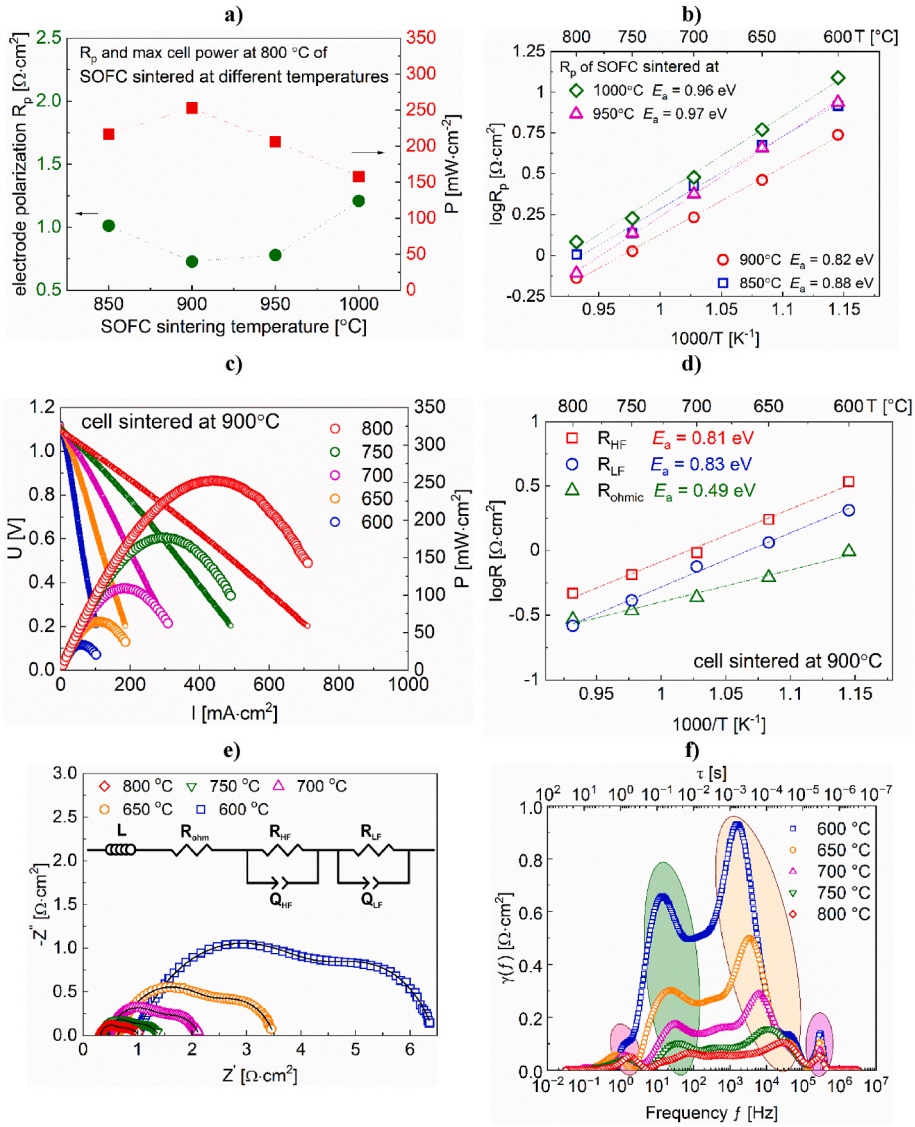

Fig. 8. (a) electrode polarization and maximum power output at 800 °C of air | $Sr_2Fe_{1.8}W_{0.2}O_{6-\delta}$ | LSGM | $Sr_2Fe_{1.6}W_{0.4}O_{6-\delta}$ |H_2 quasi-symmetrical cells with both electrodes sintered at 850−1000 °C, (b) temperature dependence of total electrode-related resistances R_p of SOFCs with electrodes sintered at 850−1000 °C, (c) voltage and power density as a function of the current density of the quasi-symmetrical cell with both electrodes sintered at 900 °C, (d) temperature dependence of ohmic resistance R_{ohmic} and electrode resistance R_{HF} (high-frequency contribution) and R_{LF} (low-frequency contribution) of SOFCs with electrodes sintered at 900 °C, (e) EIS data for the quasi-symmetrical cells sintered at 900 °C with their respective fits, (f) Results of DRT analysis of the corresponding EIS for the quasi-symmetrical cells sintered at 900 °C.

were recorded. In the case of the presence of 8YSZ, $Sr_2Fe_{2-x}W_xO_{6-\delta}$ oxides are stable with 8YSZ at 900 °C (Fig. S6 and Table S6), while additional unknown peaks which may correspond to the $SrZrO_3$ phase were detected for the compatibility studies conducted at 1000 °C (see Fig. S9), which indicates that $Sr_2Fe_{2-x}W_xO_{6-\delta}$ suffer chemical incompatibility issues with 8YSZ at high temperatures ≥1000 °C. Interestingly, as can be seen in Fig. S9, the increase of tungsten in $Sr_2Fe_{2-x}W_xO_{6-\delta}$ (x = 0.1−0.5) leads to a decrease of intensities of additional unknown peaks, showing a suppression of chemical reactions between $Sr_2Fe_{2-x}W_xO_{6-\delta}$ and 8YSZ at 1000 °C. In addition, We have investigated the chemical compatibility of $Sr_2Fe_{2-x}W_xO_{6-\delta}$ (x = 0.1−0.5) towards GDC, LSGM and 8YSZ electrolytes in reducing conditions (5 vol% H_2 in argon at 850 °C for 10 h). As shown in Fig. S10−S12 and Table S9−S10, $Sr_2Fe_{2-x}W_xO_{6-\delta}$ (x = 0.1−0.5) perovskites present excellent chemical compatibility with GDC and LSGM ceramic electrolytes under reducing condition. However, for the case with 8YSZ, $Sr_2Fe_{2-x}W_xO_{6-\delta}$ oxides react with 8YSZ in the atmosphere of 5 vol% H_2/argon. As can be seen in Fig. S12, the increase of tungsten content in $Sr_2Fe_{2-x}W_xO_{6-\delta}$ (x = 0.1−0.5) decreases the intensity of additional unknown peaks which may correspond to the $SrZrO_3$ phase, indicating a suppression of chemical reactions between $Sr_2Fe_{2-x}W_xO_{6-\delta}$ and 8YSZ under reducing condition.

For the long-term chemical stability and compatibility studies (Fig. S13−S15), the XRD data after the studies show no additional phase, confirming the good chemical stability and compatibility of $Sr_2Fe_{2-x}W_xO_{6-\delta}$ (x = 0.1−0.5) with $Ce_{0.8}Gd_{0.2}O_{1.9}$, $La_{0.8}Sr_{0.2}Ga_{0.8}Mg_{0.2}O_{3-d}$ and 8YSZ electrolytes at 800 °C for 100 h. Moreover, as can be seen in Table S11−S13, the refined unit cell parameters of $Sr_2Fe_{2-x}W_xO_{6-\delta}$ (x = 0.1−0.5) after the chemical stability and compatibility studies are very close to the results of as-synthesized materials presented in Table S1. The studies imply the possible long stable operation of solid oxide cells with $Sr_2Fe_{2-x}W_xO_{6-\delta}$ electrode materials towards typically applied electrolytes at 800 °C.

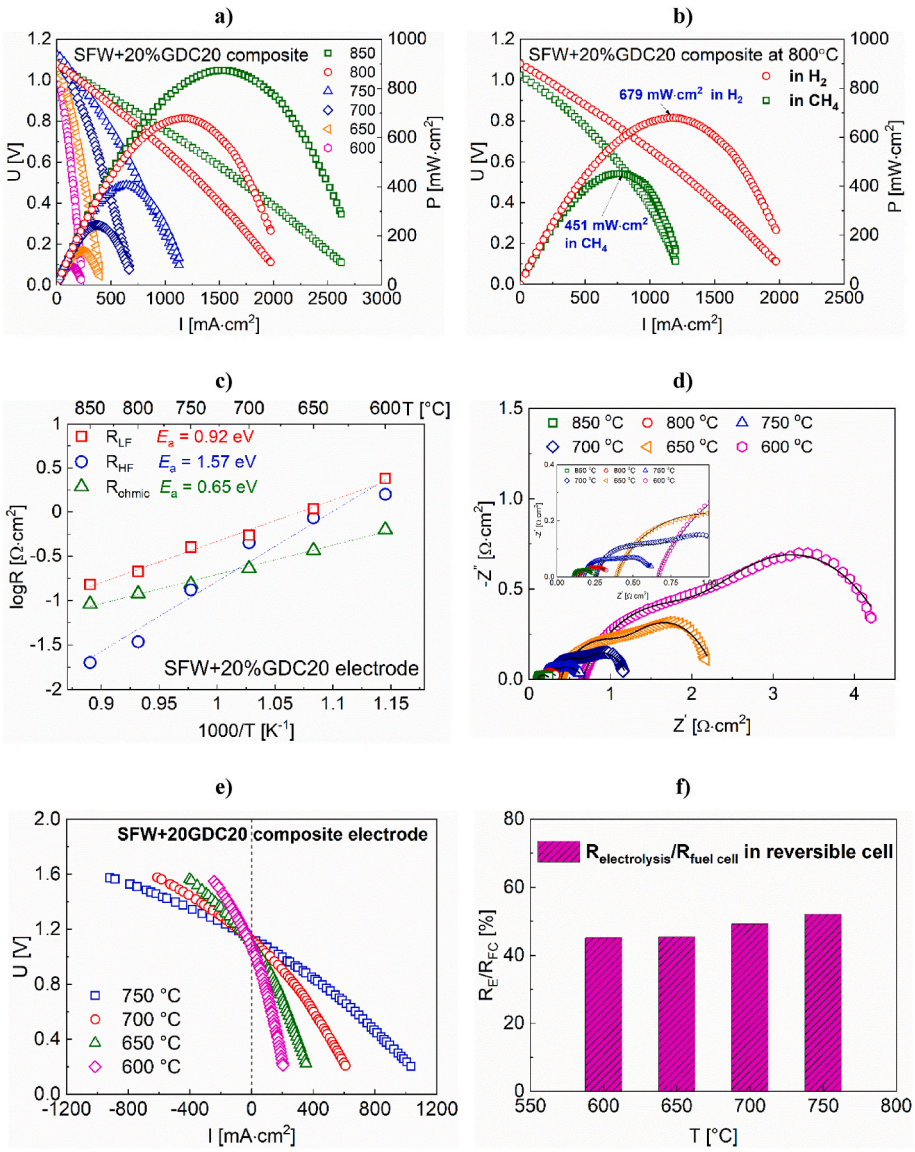

Fig. 9. (a) Voltage and power density of button−type: air | 80%$Sr_2Fe_{1.8}W_{0.2}O_{6-\delta}$+20%GDC | LSGM | 80%$Sr_2Fe_{1.6}W_{0.4}O_{6-\delta}$+20%GDC | wet H_2, quasi-symmetrical cell as a function of current density, (b) Quasi-symmetrical cell operating in CH_4 and H_2 at 800 °C, (c) Temperature dependence of ohmic R_{ohmic} and electrode-related R_{LF} and R_{HF} resistances, (d) Impedance spectra with fit for symmetrical cell as a function of temperature. Inset shows used equivalent circuit for refinement, (e) Reversible operation of 80%$Sr_2Fe_{1.8}W_{0.2}O_{6-\delta}$+20%GDC | LSGM | 80%$Sr_2Fe_{1.6}W_{0.4}O_{6-\delta}$+20%GDC (SFW+20GDC20 composite) quasi-symmetrical Solid Oxide Cells, (f) Relative ratio of performance (evaluated using respective resistance) in the electrolysis and fuel cell modes as a function of temperature.

3.5. Electrochemical impedance studies of symmetrical cells

Symmetrical cells based on LSGM electrolyte with $Sr_2Fe_{2-x}W_xO_{6-\delta}$ (x = 0.1−0.5) electrode materials were fabricated, as explained in the experimental section. The electrochemical impedance characterization of constructed symmetrical cells at 800 °C was conducted in air and 5 vol % H_2/argon, respectively (see Fig. S16). In general, $Sr_2Fe_{2-x}W_xO_{6-\delta}$ (x = 0.1−0.5) electrodes at 800 °C show much lower electrode polarizations in air (between 0.32 and 0.06 Ω cm^2) than in 5 vol% H_2 in argon (in 9.06−0.56 Ω cm^2). The lowest total cathodic polarization resistance (R_p) in the air at 800 °C was recorded for $Sr_2Fe_{1.8}W_{0.2}O_{6-\delta}$ with 0.06 Ω cm^2. While $Sr_2Fe_{1.6}W_{0.4}O_{6-\delta}$ electrode presents the smallest electrode polarization value at 800 °C in 5 vol% H_2 in argon, with 0.56 Ω cm^2. Therefore, the symmetrical cells of $Sr_2Fe_{1.8}W_{0.2}O_{6-\delta}$ and $Sr_2Fe_{1.6}W_{0.4}O_{6-\delta}$ have been systematically studied in air and 5 vol% H_2 in argon between 600 and 900 °C, as shown in Fig. 7a and b. For both $Sr_2Fe_{2-x}W_xO_{6-\delta}$ (x = 0.2 and 0.4) symmetrical cells, much lower activation energies are recorded in 5 vol% H_2/argon than in air, and $Sr_2Fe_{1.6}W_{0.4}O_{6-\delta}$ presents the lowest activation energy E_a = 0.54 eV in 5 vol% H_2/Ar, indicating the feasibility of this material as an anode candidate for SOFCs. In the case of the electrode performance in air, $Sr_2Fe_{1.8}W_{0.2}O_{6-\delta}$ exhibits a smaller activation energy (E_a = 1.23 eV) than $Sr_2Fe_{1.6}W_{0.4}O_{6-\delta}$, and an excellent electrode performance with 0.023 Ω cm^2 electrode polarization was recorded for $Sr_2Fe_{1.8}W_{0.2}O_{6-\delta}$ at 900 °C in air. Both $Sr_2Fe_{2-x}W_xO_{6-\delta}$ (x = 0.2 and 0.4) symmetrical cells show a very stable performance in air at 800 °C for 100 h (see Fig. 7c). While in 5 vol% H_2/argon, a substantial electrode performance degradation was recorded for $Sr_2Fe_{1.8}W_{0.2}O_{6-\delta}$ cell at 800 °C for 100 h, and $Sr_2Fe_{1.6}W_{0.4}O_{6-\delta}$ symmetrical cell demonstrates a stable electrode polarization value without significant degradations (see Fig. 7d). Therefore, $Sr_2Fe_{1.8}W_{0.2}O_{6-\delta}$ and $Sr_2Fe_{1.6}W_{0.4}O_{6-\delta}$ can be very excellent cathode and anode material candidates, respectively. Quasi-symmetrical SOFCs with the configuration of air | $Sr_2Fe_{1.8}W_{0.2}O_{6-\delta}$ | LSGM | $Sr_2Fe_{1.6}W_{0.4}O_{6-\delta}$ |H_2 were fabricated and comprehensively studied.

Table 3
Electrochemical performance comparison of symmetrical and quasi-symmetrical electrodes for solid oxide cells.

Cell configuration	Peak power density [mW cm^{-2}]	Electrolysis performance [mA cm^{-2}]	Ref.
80%$Sr_2Fe_{1.8}W_{0.2}O_{6-\delta}$+20%GDC | LSGM (300 μm) | 80% $Sr_2Fe_{1.6}W_{0.4}O_{6-\delta}$+20%GDC	**679** at 800 °C, **874** at 850 °C in wet H_2; **451** at 800 °C in wet CH_4	**743** at 1.5 V, 3%H_2O/H_2 at 750 °C	This work
70%$La_{0.6}Sr_{0.4}Fe_{0.8}Cu_{0.2}O_{3-\delta}$ + 30% GDC | LSGM (300 μm) | 70% $La_{0.6}Sr_{0.4}Fe_{0.8}Cu_{0.2}O_{3-\delta}$ + 30% GDC	294 at 800 °C in H_2; 110 at 800 °C (with 7% Ni infiltrated anode) in CH_4/CO_2 fuel mixture	–	[59]
$SmBaMn_2O_{5+\delta}$ | LSGM (300 μm) | $SmBaMn_2O_{5+\delta}$	481 at 800 °C in humidified H_2	–	[60]
70%$La_{0.8}Sr_{1.2}Fe_{0.9}Co_{0.1}O_{4-\delta}$+30% $Gd_{0.1}Ce_{0.9}O_{2-\delta}$ | LSGM9182 (1000 μm) | 70% $La_{0.8}Sr_{1.2}Fe_{0.9}Co_{0.1}O_{4-\delta}$+30% $Gd_{0.1}Ce_{0.9}O_{2-\delta}$	325 at 800 °C in humidified H_2	–	[61]
$Sr_2Fe_{1.5}Mo_{0.5}O_{6-\delta}$ | LSGM9182 (265 μm) | $Sr_2Fe_{1.5}Mo_{0.5}O_{6-\delta}$	500 at 800 °C in wet H_2	–	[18]
$Pr_{0.6}Sr_{0.4}FeO_{3-\delta}$ | LSGM9182 (265 μm) | $Pr_{0.6}Sr_{0.4}FeO_{3-\delta}$	591 at 800 °C in wet H_2	750 at 1.5 V, 3%H_2O/H_2 at 750 °C)	[56]
LSSMR50 | SSZ (200 μm) | LSSMR50	318 at 800 °C in wet H_2	536 at 1.5 V, 50%H_2O/H_2 at 750 °C	[57]
$Sm_{0.7}Sr_{0.2}Fe_{0.8}Ti_{0.15}Ru_{0.05}O_{3-\delta}$ | $Sm_{0.2}Ce_{0.8}O_{1.9}$ (600 μm) | $Sm_{0.7}Sr_{0.2}Fe_{0.8}Ti_{0.15}Ru_{0.05}O_{3-\delta}$	417 at 800 °C in humidified H_2		[62]
$SrFe_{0.8}W_{0.2}O_{3-\delta}$ | LSGM (300 μm) | $SrFe_{0.8}W_{0.2}O_{3-\delta}$	580 at 800 °C in humidified H_2	–	[39]
$PrBaFe_{1.6}Ni_{0.4}O_{5+\delta}$ | $Sm_{0.8}Ce_{0.2}O_{1.9}$ | $PrBaFe_2O_{5+\delta}$	120 at 650 °C in humidified H_2	–	[12]
$Pr_{0.6}Sr_{0.4}Fe_{0.8}Ni_{0.2}O_{3-\delta}$ | GDC | LSGM9182 (320 μm) | GDC | $Pr_{0.6}Sr_{0.4}Fe_{0.8}Ni_{0.2}O_{3-\delta}$	500 at 800 °C in humidified H_2	–	[63]
$PrBaMn_{1.5}Fe_{0.5}O_{5+\delta}$ | LSGM (520 μm) | $PrBaMn_{1.5}Fe_{0.5}O_{5+\delta}$	540 at 800 °C in humidified H_2	–	[64]
$La_{0.54}Sr_{0.36}Co_{0.2}Fe_{0.6}Nb_{0.2}O_{3-\delta}$ | $Ce_{0.8}Sm_{0.2}O_{1.9}$ | LSGM9182 (200 μm) | $Ce_{0.8}Sm_{0.2}O_{1.9}$ | $La_{0.54}Sr_{0.36}Co_{0.2}Fe_{0.6}Nb_{0.2}O_{3-\delta}$	539 at 800 °C in H_2	–	[65]
$Sr_2TiFe_{0.9}Mo_{0.1}O_{6-\delta}$ | $Ce_{0.8}Sm_{0.2}O_{1.9}$ | LSGM9182 (200 μm) | $Ce_{0.8}Sm_{0.2}O_{1.9}$ | $Sr_2TiFe_{0.9}Mo_{0.1}O_{6-\delta}$	444 at 800 °C in humidified H_2	–	[66]
$La_{0.7}Sr_{0.3}Fe_{0.7}Ga_{0.3}O_{3-\delta}$ | $La_{0.8}Sr_{0.2}Ga_{0.83}Mg_{0.17}O_{3-\delta}$ (320 μm) | $La_{0.7}Sr_{0.3}Fe_{0.7}Ga_{0.3}O_{3-\delta}$	489 at 800 °C in wet H_2	–	[67]
$PrBaFe_{1.8}Co_{0.2}O_{5+\delta}$ | LSGM9182 (280 μm) | $PrBaFe_{1.8}Co_{0.2}O_{5+\delta}$	563 at 800 °C in H_2	450 at 1.3 V, H_2O/CO_2 at 800 °C	[68]

LSGM: $La_{0.8}Sr_{0.2}Ga_{0.8}Mg_{0.2}O_{3-\delta}$, LSGM9182: $La_{0.9}Sr_{0.1}Ga_{0.8}Mg_{0.2}O_{2.85}$, GDC: $Ce_{0.8}Gd_{0.2}O_{1.9}$, LSSMR50: $(La_{0.8}Sr_{0.2})_{0.9}Sc_{0.2}Mn_{0.75}Ru_{0.05}O_{3-\delta}$, SSZ: Sc_2O_3 stabilized ZrO_2

3.6. High-performance quasi-symmetrical SOCs

For optimizing the sintering temperature of both electrodes for $Sr_2Fe_{1.8}W_{0.2}O_{6-\delta}$ | LSGM | $Sr_2Fe_{1.6}W_{0.4}O_{6-\delta}$ quasi-symmetrical SOFCs, the studies of sintering temperature (850−1000 °C in air) effect on the cell performance have been systematically conducted (see Figure S17 and Fig. 8). The sintering temperature of cells considerably impacts on the change of total electrode-related resistances R_p of SOFCs, while the variation of ohmic resistances is not significant. Interestingly, in all SOFCs sintered at 850−1000 °C, the electrode polarization from the high frequency contribution is dominant, indicating that the charge transfer at the electrode/electrolyte interface is the rate-limiting step of the electrode reaction [45]. As can be seen in Fig. 8a, the quasi-symmetrical SOFC sintered at 900 °C in the air presents the best cell power output of 253 mW cm^{-2} and the lowest total electrode polarization of 0.73 Ω cm^2 at 800 °C. In addition, among all SOFCs sintered at 850−1000 °C (see Fig. 8b), the cell prepared at 900 °C possesses the lowest activation energy E_a = 0.82 eV.

The distribution of relaxation times (DRT) profiles of the corresponding electrochemical impedance spectra (EIS) obtained using the DRTtools [52] are shown in Fig. 8f. Four characteristic peaks can be observed, but two main big peaks located at 10−100 Hz and 10^3−10^5 Hz are dominant, which can be illustrated as high-frequency peak and low-frequency peak, respectively. Both two predominant peaks are very sensitive to the operation temperature of cells. The peaks are shifted to a higher frequency range with the increase of temperature, and their intensities also significantly decrease. The Nyquist plots of SOFC sintered at 900 °C with fitting results and $L-R_{ohm}-(Q_{HF}-R_{HF})-(Q_{LF}-R_{LF})$ equivalent circuit in Fig. 8e show that the high frequency arc is larger than the low frequency arc. The two evident peaks from the DRT analysis also confirm the possibility to differ the low-frequency polarization R_{LF} and high-frequency polarization R_{HF} for the electrodes of cells, which were obtained and presented in Fig. 8d. It is evidently shown that the high-frequency resistances are much larger than the low-frequency polarizations, while the obtained activation energies for high-frequency resistances ($E_{a,\ HF}$ = 0.81 eV) and low-frequency resistances are very similar ($E_{a,\ LF}$ = 0.83 eV). It is reported that the high-frequency peak is associated with the charge transfer processes at electrode and electrode/electrolyte interface, while the low-frequency peak is related with the gas adsorption/dissociation process of electrode surface [39,45]. Therefore, the rate-limiting step of the electrode reaction in air | $Sr_2Fe_{1.8}W_{0.2}O_{6-\delta}$ | LSGM | $Sr_2Fe_{1.6}W_{0.4}O_{6-\delta}$ |H_2 quasi-symmetrical cells should be the charge transfer at the electrode/electrolyte interface. The fabrication of an electrode composite with additional ionic components (such as GDC or YSZ) can favor the charge transfer at the electrode/electrolyte interface, thus enhancing the SOFC performance [53,54]. Therefore, quasi-symmetrical SOCs with an additional 20 wt % $Ce_{0.8}Gd_{0.2}O_{1.9}$ composite electrodes were fabricated.

Excellent electrochemical performance was recorded in Fig. 9 for quasi-symmetrical cells with 20 wt % $Ce_{0.8}Gd_{0.2}O_{1.9}$ composite electrode in the configuration of air | 80%$Sr_2Fe_{1.8}W_{0.2}O_{6-\delta}$+20%GDC | LSGM | 80%$Sr_2Fe_{1.6}W_{0.4}O_{6-\delta}$+20%GDC | wet H_2. As shown in Fig. 9a, a very high-power output of 874 mW cm^{-2} and 679 mW cm^{-2} was documented at 850 °C and 800 °C, respectively. In addition, the cell was measured in wet CH_4 at 800 °C with a value of 451 mW cm^{-2}. The obtained maximum cell power output is one of the best results reported for symmetrical SOFCs and quasi-symmetrical cells (see Table 3). The total electrode polarization resistance (R_{HF} and R_{LF}) of the studied quasi-symmetrical cell reaches 0.17 Ω cm^2 at 850 °C and 0.25 Ω cm^2 at 800 °C, being relatively lower than other reported symmetrical SOFCs [1,2]. As shown in Fig. 9d, the low frequency arc is larger than the high frequency arc, suggesting the electrode performance is limited by the dissociative adsorption/surface diffusion process [45]. Compared with the result presented in Fig. 8d, the addition of $Ce_{0.8}Gd_{0.2}O_{1.9}$ in quasi-symmetrical cells notably reduces the electrode polarization R_{HF} associated with the high frequency (see Fig. 9c), showing the enhancement of charge transfer at the electrode/electrolyte interface with the presence of GDC in the composite electrode. The addition of an ionic component ($Ce_{0.8}Gd_{0.2}O_{1.9}$) in the SFW-GDC composite significantly enhances the oxygen incorporation kinetics of the electrode [54,55] relative to that for the pure SFW perovskite. The synergistic oxygen incorporation at the extended SFW-GDC-gas triple phase boundaries (TPBs) of the composite electrode considerably boosts the electrochemical performance of SOFCs.

In addition, the constructed quasi-symmetrical cell was also tested in the reversible operation (see Fig. 9e and f), with a slope of the characteristics being smaller for negative currents, demonstrating much smaller total polarization in the electrolysis mode. A relatively good

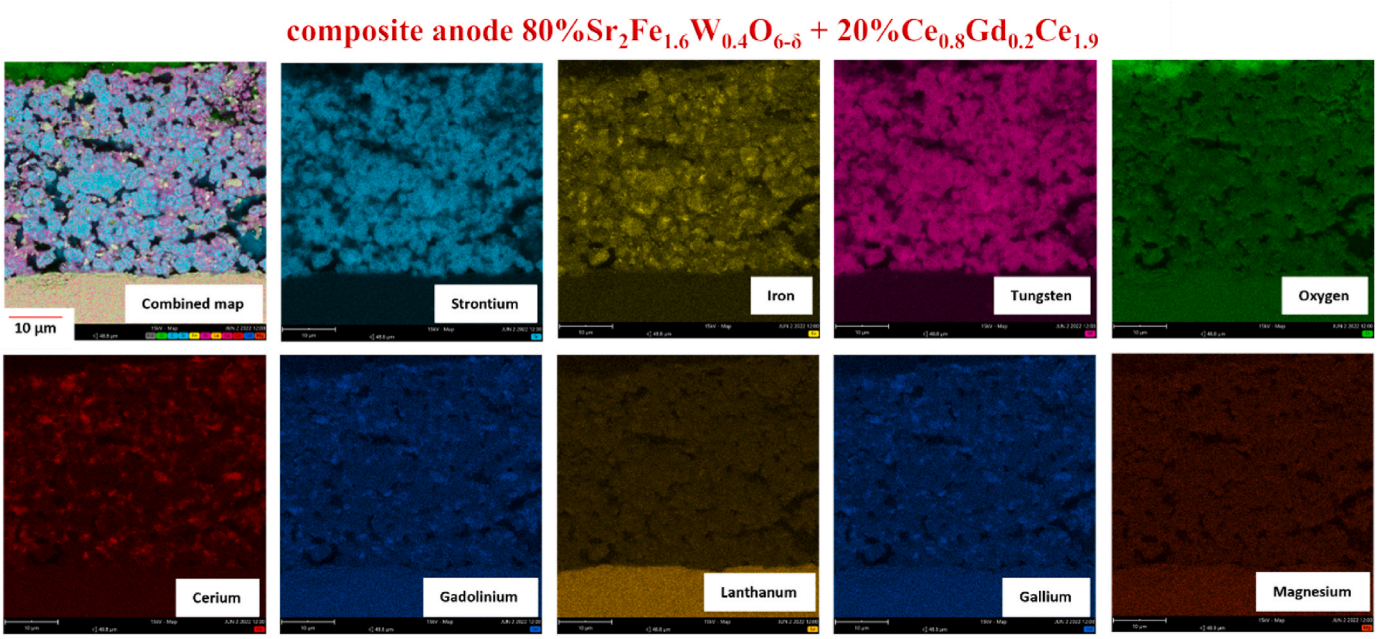

Fig. 10. EDS map of element distribution in the 80%$Sr_2Fe_{1.6}W_{0.4}O_{6-\delta}$+20%$Ce_{0.8}Gd_{0.2}O_{1.9}$ anode after cell tests.

current density of 743 mA cm^{-2} was recorded at 1.5 V in 3 vol%H_2O/H_2 at 750 °C, which is comparable with the value for $Pr_{0.6}Sr_{0.4}FeO_{3-\delta}$ | $La_{0.9}Sr_{0.1}Ga_{0.8}Mg_{0.2}O_{2.85}$ (265 μm) | $Pr_{0.6}Sr_{0.4}FeO_{3-\delta}$ symmetrical cell (750 mA cm^{-2} at 1.5 V in 3 vol% H_2O/H_2 at 750 °C) [56] and much higher than the result for $(La_{0.8}Sr_{0.2})_{0.9}Sc_{0.2}Mn_{0.75}Ru_{0.05}O_{3-\delta}$ electrode−based symmetrical cell (536 mA cm^{-2} at 1.5 V in 50 vol% H_2O/H_2 at 750 °C) [57]. The relative ratio of performance in the electrolyzer and fuel cell modes as a function of temperature, obtained from the current density-voltage slopes, is presented in Fig. 9f. Since the current density-voltage characteristics are fairly linear, the total polarization resistance ($R_0 + R_p$) of the symmetrical cell can be estimated by the mentioned slopes, either in the electrolyzer (R_E) or fuel cell (R_{FC}) modes [58]. Interestingly, as illustrated in Fig. 9f, the operation in the electrolyzer mode shows much smaller total polarization resistances, suggesting better electrocatalytic activity for the electrolyzer process of the electrochemical reactions. While the electrolyzer performance of fabricated quasi-symmetrical cells still needs further investigation.

3.7. *Post-mortem analysis of electrodes and in situ exsolution of metallic nanoparticles*

The post-mortem SEM analysis with energy dispersive X-ray spectroscopy (EDS) for the composite cathode and anode show well mixed composite electrode with $Ce_{0.8}Gd_{0.2}O_{1.9}$ and a homogenous distribution of electrode materials and $Ce_{0.8}Gd_{0.2}O_{1.9}$ (see Fig. 10, Figs. S9 and S10). Agglomerates with the size of 5 μm can be observed for cathode materials (Fig. S18), while the agglomerates in anode have a smaller size, around 2.5 μm (Fig. 10). The electrode has a porous microstructure, and both anode and cathode possess good adhesion to the electrolyte (see the cross-section view of electrodes in Fig. S19).

As can be observed in Fig. 11a, *in situ* exsolved nanoparticles have been detected on the surface of $Sr_2Fe_{1.6}W_{0.4}O_{6-\delta}$ anode. The nanoparticles are seen dispersed on the surface of the anode material in the secondary electron (SE) SEM mode. For more insightful analysis the material was examined by TEM studies (Figure S20 and Fig. 11). Nanoparticles are easily visible from the STEM high-angle annular dark-field (HAADF) images in Fig. 11 a. The size of nanoparticles is estimated at ≤ 20 nm. The nanoparticles appear mainly near the grain boundaries. The EDS elemental distribution mapping confirms the exsolved nanoparticles are enriched in Fe (Fig. 11a). In addition, an overview STEM-HAADF image of the second thin foil cut out from the same anode sample is shown in Fig. S21. The second foil was cut from the cross-section. In Fig. S21, STEM HAADF given alongside the EDS elemental distribution maps shows non-uniform composition concerning Fe. The chemical composition analysis confirms the rich Fe content in the *in situ* exsolved nanoparticles areas, and the results are provided in Table S14.

To investigate the structural identity of the *in situ* exsolved nanoparticles, high-resolution TEM (HRTEM) was conducted. An example HRTEM image is shown in Fig. 11b together with Fast Fourier Transform (FFT) pattern (inset). The FFT was taken from the small area marked with the red square. The FFT corresponds to α-Fe along the [111] zone axis, thus confirming that the *in situ* exsolved nanoparticles are metallic Fe. Furthermore, the electron diffraction pattern (SADP) taken from the parent $Sr_2Fe_{1.4}W_{0.6}O_6$ anode and given together with the corresponding bright field image (BF) (Fig. 11c) shows that $Sr_2Fe_{1.4}W_{0.6}O_6$ maintains the perovskite structure. The *in situ* exsolved metallic iron nanoparticles on the surface of $Sr_2Fe_{1.4}W_{0.6}O_6$ anode can be effective nanocatalysts for the fuel oxidation reaction [69], therefore, benefiting the performance of cells.

As depicted in Fig. 12, the dissolution of iron nanoparticles to the parent perovskite has been observed after the oxidation of $Sr_2Fe_{1.6}W_{0.4}O_6$ anode in the air at 900 °C for 12 h, confirming the reversibility of exsolution and dissolution of iron nanoparticles. In addition, the sample was treated in pure H_2 at 800 °C for 12 h, and the re-exsolution of nanoparticles can also be detected. Similarly, the reversible exsolution and dissolution of nanoparticles have also been reported in the Co-doped $Sr_2Fe_{1.5}Mo_{0.5}O_{6-\delta}$ system [70].

4. Conclusions

In this work, we have provided a new design approach of high-performance quasi-symmetrical Solid Oxide Cells by employing a facile chemical modification strategy for $Sr_2Fe_{2-x}W_xO_{6-\delta}$ electrode materials with *in situ* exsolved nanoparticles decorated on the anode. The tungsten content in $Sr_2Fe_{2-x}W_xO_{6-\delta}$ significantly determines the physicochemical and electrochemical properties. Low content $Sr_2Fe_{2-x}W_xO_{6-\delta}$ (x = 0.1−0.5) oxides present simple perovskite structure with *Pm-3m* space group and excellent redox stability, while the increase of tungsten in $Sr_2Fe_{2-x}W_xO_{6-\delta}$ (x = 0.6−1.0) leads to the obligation of sintering materials only in reducing condition, and the

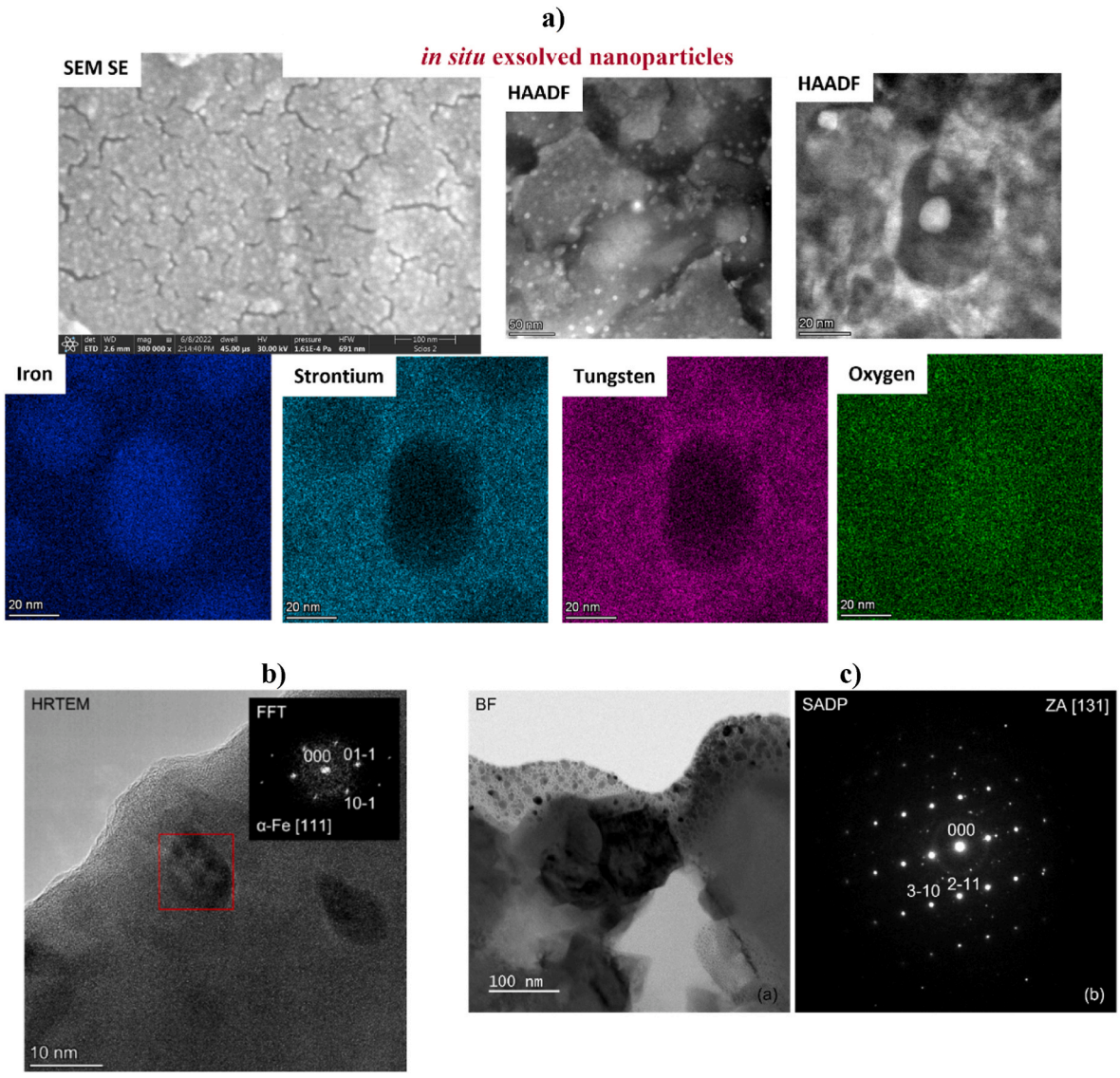

Fig. 11. (a) SEM image and STEM−HAADF images of the $Sr_2Fe_{1.4}W_{0.6}O_6$ thin foil sample and the corresponding elemental distribution maps, (b) High resolution (HRTEM) image with the Fast Fourier Transform (inset) taken from the exsolved nanoparticle from $Sr_2Fe_{1.4}W_{0.6}O_6$, (c) the bright field image (BF) and the corresponding electron diffraction pattern (SADP) taken from the parent $Sr_2Fe_{1.4}W_{0.6}O_6$ anode.

revolution of crystal structure to $P2_1/n$ space group. The maximum doping level of W in $Sr_2Fe_{2-x}W_xO_{6-\delta}$ is determined to be limited to x = 1.0. The ab initio theoretical calculations indicate the substitution of Fe with W in $Sr_2Fe_{2-x}W_xO_{6-\delta}$ perovskites lead to a decrease in conductivity, which was confirmed by the experimental studies of electrical conductivity. In addition, the increased content of W in $Sr_2Fe_{2-x}W_xO_{6-\delta}$ (x = 0.1−0.5) oxides decreases the oxygen content change and thermal expansion coefficients, as well as the relative unit cell volume change between reduced and oxidized compounds. All $Sr_2Fe_{2-x}W_xO_{6-\delta}$ compounds show excellent redox stability and chemical compatibility with mostly used solid electrolytes. Among all studied symmetrical cells with $Sr_2Fe_{2-x}W_xO_{6-\delta}$ (x = 0.1−0.5) electrodes, $Sr_2Fe_{1.8}W_{0.2}O_{6-\delta}$ and $Sr_2Fe_{1.6}W_{0.4}O_{6-\delta}$ electrodes present the smallest electrode polarization in air (R_p = 0.06 Ω cm^2 at 800 °C for 100 h) and in reducing condition (Rp = 0.56 Ω cm^2 at 800 °C in 5 vol% H_2/Ar for 100 h), respectively. We have demonstrated a high-performance quasi-symmetrical solid oxide cell with the configuration of 80%$Sr_2Fe_{1.8}W_{0.2}O_{6-\delta}$+20%GDC | LSGM | 80%$Sr_2Fe_{1.6}W_{0.4}O_{6-\delta}$+20%GDC, showing high power outputs with 874 mW cm^{-2} at 850 °C in wet H_2 and good current density of 743 mA cm^{-2} at 1.5 V in electrolysis mode at 750 °C. In addition, the cell was measured in wet CH_4 at 800 °C with a value of 451 mW cm^{-2}. The anode surface of $Sr_2Fe_{1.6}W_{0.4}O_{6-\delta}$ is decorated with *in situ* exsolved metallic iron nanoparticles, which contribute to the excellent electrochemical performance of cells. This study demonstrates a new design scenario for high-performance symmetrical Solid Oxide Cells that uses a simple chemical modification strategy for electrode materials with *in situ* exsolved nanocatalysts.

CRediT authorship contribution statement

Kun Zheng: Conceptualization, Methodology, Investigation, Data curation, Visualization, Writing – original draft, Supervision, Funding acquisition. **Jakub Lach:** Methodology, Investigation, Data curation, Visualization. **Paweł Czaja:** Methodology, SEM and TEM studies. **Michał Gogacz:** Methodology. **Patryk Czach:** Investigation, Formal analysis. **Agnieszka Brzoza-Kos:** Investigation, SEM/EDS. **Piotr Winiarz:** DFT calculations. **Jie Luo:** Formal analysis, Writing - review.

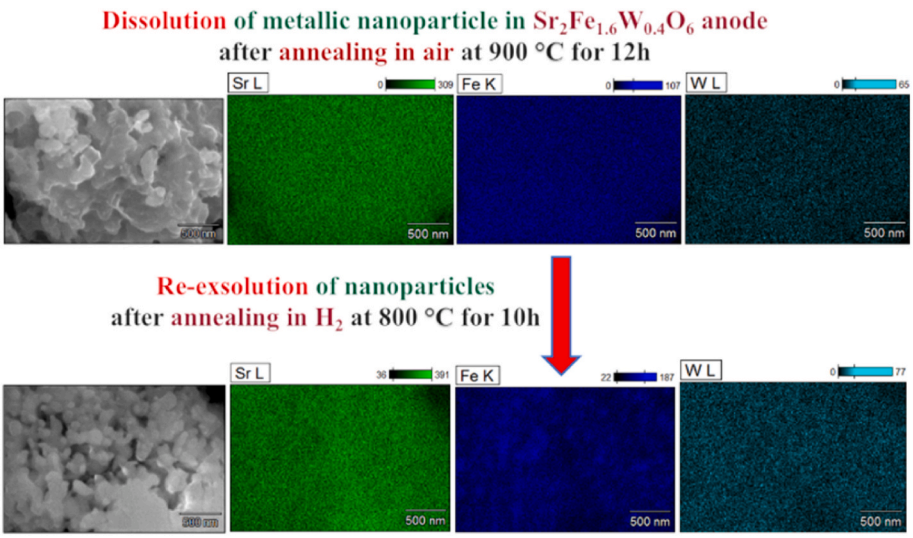

Fig. 12. The dissolution and re−exsolution of nanoparticles on the $Sr_2Fe_{1.6}W_{0.4}O_6$ anode.

Declaration of competing interest

The authors declare that they have no known competing financial interests or personal relationships that could have appeared to influence the work reported in this paper.

Data availability

Data will be made available on request.

Acknowledgments

The work was funded by the National Science Centre Poland (NCN) based on the decision number UMO-2021/43/D/ST5/00824.

Supporting Information

Rietveld refinement results for $Sr_2Fe_{2-x}W_xO_{6-\delta}$ (x = 0.1 to 1) oxides; Thermal expansion behavior of $Sr_2Fe_{2-x}W_xO_{6-\delta}$ (x = 0.1−0.5) materials in the air; selected electrical conductivity values of $Sr_2Fe_{2-x}W_xO_{6-\delta}$ (x = 0.1−0.5) materials in the air between 600 and 800 °C; XRD data with Rietveld refinement and the refinement results for $Sr_2Fe_{2-x}W_xO_{6-\delta}$ after the reduction in 5 vol% H_2 in argon for 100 h at 800 °C; SEM micrographs of $Sr_2Fe_{2-x}W_xO_{6-\delta}$ powders after the reduction at 800 °C for 100 h in 5 vol% H_2 in argon; XRD data with Rietveld refinement and the refinement results for 50:50 wt% mixtures of typical electrolyte ($Ce_{0.8}Gd_{0.2}O_{1.9}$, $La_{0.8}Sr_{0.2}Ga_{0.8}Mg_{0.2}O_{3-d}$ and 8YSZ) and $Sr_2Fe_{2-x}W_xO_{6-\delta}$ after the chemical stability and compatibility studies; Electrode polarizations of symmetrical cells with $Sr_2Fe_{2-x}W_xO_{6-\delta}$ (x = 0.1−0.5) electrodes measured at 800 °C in air and in 5 vol% H_2/argon; Power output and polarizations of air | $Sr_2Fe_{1.8}W_{0.2}O_{6-\delta}$ | LSGM | $Sr_2Fe_{1.6}W_{0.4}O_{6-\delta}$ |H_2 cells with electrodes sintered at 850−1000 °C; SEM micrographs with EDS mapping of cathode and anode, as well as cross-section view for measured cells; STEM-HAADF studies of the thin foil cut out from the $Sr_2Fe_{1.4}W_{0.6}O_6$ sample together with the EDS analysis.

Appendix A. Supplementary data

Supplementary data to this article can be found online at https://doi.org/10.1016/j.jpowsour.2023.233707.

References

[1] M. Zhang, Z. Du, Y. Zhang, H. Zhao, Progress of perovskites as electrodes for symmetrical solid oxide fuel cells, ACS Appl. Energy Mater. 11 (2022) 13081–13095.
[2] J. Zamudio-García, L. Caizan-Juanarena, J.M. Porras-Vazquez, E.R. Losilla, D. Marrero-Lopez, A review on recent advances and trends in symmetrical electrodes for solid oxide cells, J. Power Sources 520 (2022), 230852.
[3] K. Zhu, B. Luo, Z. Liu, X. Wen, Recent advances and prospects of symmetrical solid oxide fuel cells, Ceram. Int. 48 (2022) 8972–8986.
[4] J.C. Ruiz-Morales, D. Marrero-López, J. Canales-Vazquez, J.T.S. Irvine, Symmetric and reversible solid oxide fuel cells, RSC Adv. 1 (2011) 1403–1414.
[5] C. Su, W. Wang, M. Liu, M.O. Tadé, Z. Shao, Progress and prospects in symmetrical solid oxide fuel cells with two identical electrodes, Adv. Energy Mater. 5 (2015), 1500188.
[6] D.M. Bastidas, S. Tao, J.T.S. Irvine, A symmetrical solid oxide fuel cell demonstrating redox stable perovskite electrodes, J. Mater. Chem. 16 (2006) 1603–1605.
[7] L. Santos-Gomez, J.M. Porras-Vazquez, E.R. Losilla, D. Marrero-Lopez, Ti-doped $SrFeO_3$ nanostructured electrodes for symmetric solid oxide fuel cells, RSC Adv. 5 (2015) 107889–107895.
[8] W.Y.W. Anasuhah, N.A. Baharuddin, M.R. Somalu, A. Muchtar, N.P. Brandon, H. Fan, Recent advances and influencing parameters in developing electrode materials for symmetrical solid oxide fuel cells, Int. J. Miner. Metall. Mater. 30 (2023) 1–24.
[9] D. Zhang, Y. Wang, Y. Peng, Y. Luo, T. Liu, W. He, F. Chen, M. Ding, Novel high-entropy perovskite-type symmetrical electrode for efficient and durable carbon dioxide reduction reaction, Adv. Powder Mater. 2 (4) (2023), 100129.
[10] T. Liu, Y. Zhao, X. Zhang, H. Zhang, G. Jiang, W. Zhao, J. Guo, F. Chen, M. Yan, Y. Zhang, Y. Wang, Robust redox-reversible perovskite type steam electrolyser electrode decorated with in situ exsolved metallic nanoparticles, J. Mater. Chem. A 8 (2020) 582–591.
[11] Y. Zhang, X. Zhang, J. Ni, C. Ni, Pr-doped $SrTi_{0.5}Mn_{0.5}O_{3-\delta}$ as an electrode material for a quasi-symmetrical solid oxide fuel cell using methane and propane fuel, ACS Appl. Mater. Interfaces 15 (3) (2023) 3974–3984.
[12] Y. Chen, Z. Cheng, Y. Yang, Q. Gu, D. Tian, X. Lu, W. Yu, B. Lin, Novel quasi-symmetric solid oxide fuel cells with enhanced electrochemical performance, J. Power Sources 310 (2016) 109–117.
[13] J. Molenda, K. Świerczek, W. Zając, Functional materials for the IT-SOFC, J. Power Sources 173 (2007) 657–670.
[14] F.S. Silva, T.M. Souza, Novel materials for solid oxide fuel cell technologies: a literature review, Int. J. Hydrogen Energy 42 (41) (2017) 26020–26036.
[15] A. Ndubuisi, S. Abouali, K. Singh, V. Thangadurai, Recent advances, practical challenges, and perspectives of intermediate temperature solid oxide fuel cell cathodes, J. Mater. Chem. A 10 (2022) 2196.
[16] K. Zheng, K. Świerczek, Evaluation of W-containing $Sr_{1-x}Ba_xFe_{0.75}W_{0.25}O_{3-\delta}$ (x = 0, 0.5, 1) anode materials for solid oxide fuel cells, Solid State Ionics 288 (2016) 124–129.
[17] K. Zheng, K. Świerczek, J.M. Polfus, M.F. Sunding, M. Pishahang, T. Norby, Carbon deposition and sulfur poisoning in $SrFe_{0.75}Mo_{0.25}O_{3-\delta}$ and $SrFe_{0.5}Mn_{0.25}Mo_{0.25}O_{3-\delta}$ electrode materials for symmetrical SOFCs, J. Electrochem. Soc. 162 (2015) F1078–F1087, https://doi.org/10.1149/2.0981509jes.
[18] Q. Liu, X. Dong, G. Xiao, F. Zhao, F. Chen, A novel electrode material for symmetrical SOFCs, Adv. Mater. 22 (2010) 5478–5482.

[19] B.-K. Lai, K. Kerman, S. Ramanathan, Nanostructured $La_{0.6}Sr_{0.4}Co_{0.8}Fe_{0.2}O_3$/$Y_{0.08}Zr_{0.92}O_{1.96}$/$La_{0.6}Sr_{0.4}Co_{0.8}Fe_{0.2}O_3$ (LSCF/YSZ/LSCF) symmetric thin film solid oxide fuel cells, J. Power Sources 196 (2011) 1826–1832.

[20] Y. Lu, H. Zhao, X. Chang, X. Du, K. Li, Y. Ma, S. Yi, Z. Du, K. Zheng, K. Świerczek, Novel cobalt-free $BaFe_{1-x}Gd_xO_{3-\delta}$ perovskite membranes for oxygen separation, J. Mater. Chem. A 4 (2016) 10454–10466, https://doi.org/10.1039/C6TA01749E.

[21] Y. Lu, H. Zhao, X. Cheng, Y. Jia, X. Du, M. Fang, Z. Du, K. Zheng, K. Świerczek, Investigation of In-doped $BaFeO_{3-\delta}$ perovskite−type oxygen permeable membranes, J. Mater. Chem. A 3 (2015) 6202–6214.

[22] S. Kumar, A. Das, S. Omar, Electrochemical performance of $SrFeO_{3-\delta}$ for application as a symmetric electrode in solid oxide fuel cells, ACS Appl. Energy Mater. 6 (3) (2023) 2049–2062.

[23] A.J. Fernández-Ropero, J.M. Porras-Vázquez, A. Cabeza, P.R. Slater, D. Marrero-López, E.R. Losilla, High valence transition metal doped strontium ferrites for electrode materials in symmetrical SOFCs, J. Power Sources 249 (2014) 405–413.

[24] K. Zheng, K. Świerczek, Physicochemical properties of rock salt-type ordered Sr_2MMoO_6 (M = Mg, Mn, Fe, Co, Ni) double perovskites, J. Eur. Ceram. Soc. 34 (2014) 4273–4284.

[25] P. Qiu, S. Sun, J. Li, L. Jia, A review on the application of $Sr_2Fe_{1.5}Mo_{0.5}O_6$-based oxides in solid oxide electrochemical cells, Sep. Purif. Technol. 298 (2022), 121581.

[26] A. Hartley, M. Sahibzada, M. Weston, I.S. Metcalfe, D. Mantzavinos, $La_{0.6}Sr_{0.4}Co_{0.2}Fe_{0.8}O_3$ as the anode and cathode for intermediate temperature solid oxide fuel cells, Catal. Today Off. 55 (2000) 197–204.

[27] J.M. Porras-Vazquez, T. Pike, C.A. Hancock, J.F. Marco, F.J. Berry, P.R. Slater, Investigation into the effect of Si doping on the performance of $SrFeO_{3-\delta}$ SOFC electrode materials, J. Mater. Chem. A 1 (2013) 11834–11841, https://doi.org/10.1039/C3TA12113E.

[28] L. Santos-Gomez, J.M. Compana, S. Bruque, E.R. Losilla, D. Marrero-Lopez, Symmetric electrodes for solid oxide fuel cells based on Zr-doped $SrFeO_{3-\delta}$, J. Power Sources 279 (2015) 419–427.

[29] O.A. Savinskaya, A.P. Nemudry, A.N. Nadeev, S.V. Tsybuly, Synthesis and study of the thermal stability of $SrFe_{1-x}M_xO_{3-z}$ (M = Mo, W) perovskites, Solid State Ionics 179 (2008) 1076–1079.

[30] A.C. Larson, R.B. Von Dreele, General structure analysis system (GSAS), Los Alamos Natl. Lab. Rep. − LAUR (2004) 86–748.

[31] B.H. Toby, EXPGUI, a graphical user interface for GSAS, J. Appl. Crystallogr. 34 (2001) 210–213.

[32] D. Stroud, Generalized effective-medium approach to the conductivity of an inhomogeneous material, Phys. Rev. B 12 (1975) 3368–3373.

[33] J.P. Perdew, K. Burke, M. Ernzerhof, Generalized gradient approximation made simple, Phys. Rev. Lett. 77 (1996) 3865.

[34] T. Su, Y. Li, Y. Yang, Z. Xu, N. Shi, Y. Wan, Y. Xie, D. Huan, S. Xue, C. Xia, Effect of tungsten doping on strontium ferrite electrode for symmetrical solid oxide electrochemical cell, Int. J. Hydrogen Energy 45 (2020) 23401–23410.

[35] J. Gong, C. Yang, J. Zhang, W. Pu, Origin of photocatalytic activity of W/N-codoped TiO_2: H_2 production and DFT calculation with GGA+U, Appl. Catal. B Environ. 152−153 (2014) 73–81.

[36] M. Pavone, A.M. Ritzmann, E.A. Carter, Quantum-mechanics-based design principles for solid oxide fuel cell cathode materials, Energy Environ. Sci. 4 (2011) 4933–4937.

[37] H. Falcon, J.A. Barbero, J.A. Alonso, M.J. Martınez-Lope, J.L.G. Fierro, $SrFeO_{3-\delta}$ perovskite oxides: chemical features and performance for methane combustion, Chem. Mater. 14 (2002) 2325–2333.

[38] C. Yao, H. Zhang, X. Liu, J. Meng, J. Meng, F. Meng, A niobium and tungsten co-doped $SrFeO_{3-\delta}$ perovskite as cathode for intermediate temperature solid oxide fuel cells, Ceram. Int. 45 (2019) 7351–7358.

[39] Y. Cao, Z. Zhu, Y. Zhao, W. Zhao, Z. Wei, T. Liu, Development of tungsten stabilized $SrFe_{0.8}W_{0.2}O_{3-\delta}$ material as novel symmetrical electrode for solid oxide fuel cells, J. Power Sources 455 (2020), 227951.

[40] M. Retuerto, F. Jimenez-Villacorta, M.J. Martinez-Lope, Y. Huttel, E. Roman, M. T. Fernandez-Diac, J.A. Alonso, Study of the valence state and electronic structure in Sr_2FeMO_6 (M = W, Mo, Re and Sb) double perovskites, Phys. Chem. Chem. Phys. 12 (2010) 13616–13625.

[41] H. Kawanaka, I. Hase, S. Toyama, Y. Nishihara, Iron spin state of double perovskite oxide Sr_2FeWO_6, Phys. B Condens. Matter 281−282 (2000) 518–520.

[42] W. Li, D. Li, X. Gao, A. Gurlo, S. Zander, P. Jones, A. Navrotsky, Z. Shen, R. Riedel, E. Ionescu, A study on the thermal conversion of scheelite-type ABO_4 into perovskite-type $AB(O,N)_3$, Dalton Trans. 44 (2015) 8238–8246.

[43] K. Zheng, K. Świerczek, W. Zając, A. Klimkowicz, Rock salt ordered-type double perovskite anode materials for solid oxide fuel cells, Solid State Ionics 257 (2014) 9–16.

[44] H. Ullman, N. Trofimenko, Estimation of effective ionic radii in highly defective perovskite-type oxides from experimental data, J. Alloys Compd. 316 (2001) 153–158.

[45] K. Zheng, Ti-doped $Sr_2Fe_{1.4-x}Ti_xMo_{0.6}O_{6-\delta}$ double perovskites with improved stability as anode materials for Solid Oxide Fuel Cells, Mater. Res. Bull. 128 (2020), 110877.

[46] M.V. Patrakeev, I.A. Leonidov, V.L. Kozhevnikov, V.V. Kharton, Ion-electron transport in strontium ferrites: relationships with structural features and stability, Solid State Sci. 6 (2004) 907–913.

[47] X. Lia, H. Zhao, F. Gao, Z. Zhu, N. Chen, W. Shen, Synthesis and electrical properties of Co-doped $Y_{0.08}Sr_{0.92}TiO_{3-\delta}$ as a potential SOFC anode, Solid State Ionics 179 (2008) 1588–1592.

[48] C. Nicollet, H.L. Tuller, Perspective on the relationship between the acidity of perovskite oxides and their oxygen surface exchange kinetics, Chem. Mater. 34 (2022) 991–997.

[49] C. Nicollet, C. Toparli, G.F. Harrington, T. Defferriere, B. Yildiz, H.L. Tuller, Acidity of surface-infiltrated binary oxides as a sensitive descriptor of oxygen exchange kinetics in mixed conducting oxides, Nat. Catal. 3 (2020) 913–920.

[50] C. Didier, J. Claridge, M. Rosseinsky, Crystal structure of brownmillerite Ba_2InGaO_5, J. Solid State Chem. 218 (2014) 38–43.

[51] O.L. Pineda, Z.L. Moreno, P. Roussel, K. Świerczek, G.H. Gauthier, Synthesis and preliminary study of the double perovskite $NdBaMn_2O_{5+\delta}$ as symmetric SOFC electrode material, Solid State Ionics 288 (2016) 61–67.

[52] T.H. Wan, M. Saccoccio, C. Chen, F. Ciucci, Influence of the discretization methods on the distribution of relaxation times deconvolution: implementing radial basis functions with DRTtools, Electrochim. Acta 184 (2015) 483–499.

[53] X. Zhang, Y. Zheng, Z. Ding, G. Yang, X. Xiao, M. Peng, M. Wu, J. Li, J. Liu, A. Alodhay, X. Fu, Z. Shao, Y. Sun, Nanoscale intertwined biphase Nanofiber as active and durable air electrode for solid oxide electrochemical cells, ACS Sustainable Chem. Eng. 11 (23) (2023), 8592−8602.

[54] Y. Wang, B. Hu, Z. Zhu, H.J.M. Bouwmeester, C. Xia, Electrical conductivity relaxation of $Sr_2Fe_{1.5}Mo_{0.5}O_{6-\delta}$-$Sm_{0.2}Ce_{0.8}O_{1.9}$ dual-phase composites, J. Mater. Chem. A 2 (2014) 136–143, https://doi.org/10.1039/C3TA12787G.

[55] Y. Choi, H. Cho, J. Kim, J. Kang, J. Seo, J.H. Kim, S.J. Jeong, D. Lim, I. Kim, W. Jung, Nanofiber composites as highly active and robust anodes for direct-hydrocarbon solid oxide fuel cells, ACS Nano 16 (9) (2022), 14517−14526.

[56] Y. Yang, Y. Wu, H. Bao, W. Song, H. Ni, D. Tian, B. Lin, P. Feng, Y. Ling, An efficient and prospective self-assembled hybrid electrocatalyst for symmetrical and reversible solid oxide cells, Electrochim, Acta 362 (2020), 137171.

[57] J. Zhou, N. Wang, J. Cui, J. Wang, J. Yang, Z. Zong, Z. Zhang, Q. Chen, X. Zheng, K. Wu, Structural and electrochemical properties of B-site Ru-doped $(La_{0.8}Sr_{0.2})_{0.9}Sc_{0.2}Mn_{0.8}O_{3-\delta}$ as symmetrical electrodes for reversible solid oxide cells, J. Alloys Compd. 792 (2019) 1132–1140.

[58] W. Skubida, K. Zheng, A. Stępień, K. Świerczek, A. Klimkowicz, $SrCe_{0.9}In_{0.1}O_{3-\delta}$−based reversible symmetrical Protonic Ceramic Cell, Mater. Res. Bull. 135 (2021), 111154.

[59] F. Zurlo, I.N. Sora, V. Felice, I. Luisetto, C. D'Ottavi, S. Licoccia, E.D. Bartolomeo, Copper-doped lanthanum ferrites for symmetric SOFCs, Acta Mater. 112 (2016) 77–83.

[60] Y. Zhang, H. Zhao, Z. Du, K. Świerczek, Y. Li, High-performance $SmBaMn_2O_{5+\delta}$ electrode for symmetrical solid oxide fuel cell, Chem. Mater. 31 (2019) 3784–3793.

[61] J. Zhou, T. Shin, C. Ni, G. Chen, K. Wu, Y. Cheng, J.T.S. Irvine, In situ growth of nanoparticles in layered perovskite $La_{0.8}Sr_{1.2}Fe_{0.9}Co_{0.1}O_{4-\delta}$ as an active and stable electrode for symmetrical solid oxide fuel cells, Chem. Mater. 28 (2016) 2981–2993.

[62] W. Fan, Z. Sun, Y. Bai, K. Wu, Y. Cheng, Highly stable and efficient perovskite ferrite electrode for symmetrical solid oxide fuel cells, ACS Appl. Mater. Interfaces 11 (2019) 23168–23179.

[63] X. Lu, Y. Yang, Y. Ding, Y. Chen, Q. Gu, D. Tian, W. Yu, B. Lin, Mo-doped $Pr_{0.6}Sr_{0.4}Fe_{0.8}Ni_{0.2}O_{3-\delta}$ as potential electrodes for intermediate-temperature symmetrical solid oxide fuel cells, Electrochim, Acta 227 (2017) 33–40.

[64] L. Zhao, K. Chen, Y. Liu, B. He, A novel layered perovskite as symmetric electrode for direct hydrocarbon solid oxide fuel cells, J. Power Sources 342 (2017) 313–319.

[65] B. Niu, F. Jin, T. Feng, L. Zhang, Y. Zhang, T. He, A-site deficient $(La_{0.6}Sr_{0.4})_{1-x}Co_{0.2}Fe_{0.6}Nb_{0.2}O_{3-\delta}$ symmetrical electrode materials for solid oxide fuel cells, Electrochim. Acta 270 (2018) 174–182.

[66] B. Niu, F. Jin, L. Zhang, P. Shen, T. He, Performance of double perovskite symmetrical electrode materials $Sr_2TiFe_{1-x}Mo_xO_{6-\delta}$ (x = 0.1, 0.2) for solid oxide fuel cells, Electrochim. Acta 263 (2018) 217–227.

[67] Z. Yang, Y. Chen, C. Jin, G. Xiao, M. Han, F. Chen, $La_{0.7}Sr_{0.3}Fe_{0.7}Ga_{0.3}O_{3-\delta}$ as electrode material for a symmetrical solid oxide fuel cell, RSC Adv. 5 (2015) 2702–2705, https://doi.org/10.1039/c4ra11358f.

[68] C. Lu, B. Niu, W. Yi, Y. Ji, B. Xu, Efficient symmetrical electrodes of $PrBaFe_{2-x}Co_xO_{5+\delta}$ (x = 0, 0.2,0.4) for solid oxide fuel cells and solid oxide electrolysis cells, Electrochim, Acta 358 (2020), 136916.

[69] K. Kousi, C. Tang, I.S. Metcalfe, D. Neagu, Emergence and future of exsolved materials, Small 17 (2021), 2006479.

[70] H. Lv, L. Lin, X. Zhang, Y. Song, H. Matsumoto, C. Zeng, N. Ta, W. Liu, D. Gao, G. Wang, X. Bao, In situ investigation of reversible exsolution/dissolution of CoFe Alloy nanoparticles in a Co-doped $Sr_2Fe_{1.5}Mo_{0.5}O_{6-\delta}$ cathode for CO_2 electrolysis, Adv. Mater. 32 (2020), 1906193.